REVISION 2

Origin of ß-cristobalite in Libyan Desert Glass– the hottest naturally occurring silica polymorph?

Aaron J. Cavosie[1,§,†], William D.A. Rickard[2], Noreen J. Evans[1,2], Kai Rankenburg[2], Malcolm Roberts[3], Catherine A. Macris[4], and Christian Koeberl[5]

[1]School of Earth and Planetary Sciences ([§]Space Science and Technology Centre, [†]The Institute for Geoscience Research), Curtin University, Perth, WA 6102, Australia.

[2]John de Laeter Centre, Curtin University, Perth, WA 6102, Australia.

[3]Centre for Microscopy, Characterisation, and Analysis, University of Western Australia, Perth, WA 6009

[4]School of Science, Indiana University– Purdue University, Indianapolis, IN 46202, USA

[5]Department of Lithospheric Research, University of Vienna, Althanstrasse 14, A-1090 Vienna, Austria

Corresponding author Email: aaron.cavosie@curtin.edu.au

ABSTRACT

Identifying and determining the origin of ß-cristobalite, a high-temperature silica polymorph, in natural samples is challenging as it is rarely, if ever, preserved due to polymorphic transformation to α-cristobalite at low temperature. Formation mechanisms for ß-cristobalite in high silica rocks are difficult to discern, as superheating, supercooling, bulk composition, and trace element abundance all influence whether cristobalite crystallizes from melt or by

devitrification. Here we report a study of α-cristobalite in Libyan Desert Glass (LDG), a nearly pure silica natural glass of impact origin found in western Egypt, using electron microprobe analysis (EMPA), laser ablation inductively coupled mass spectrometry (LAICPMS), time-of-flight secondary ion mass spectrometry (ToF-SIMS), scanning electron microscopy (SEM), and electron backscatter diffraction (EBSD). The studied grains are mostly 250 μm in diameter, and consist of ~150 μm-wide cores surrounded by ~50 μm-wide dendritic rims. Compositional layering in LDG continues across cristobalite grains, and mostly corresponds to variations in Al content. However, layering is disrupted in cores of cristobalite grains, where Al distribution records oscillatory growth zoning, whereas in rims, high Al occurs along grain boundaries. Cristobalite cores thus nucleated within layered LDG at conditions that allowed mobility of Al into crystallographically–controlled growth zones, whereas rims grew when Al was less mobile. Analysis of 37 elements indicates little evidence of preferential partitioning; both LDG and cristobalite are variably depleted relative to upper continental crust, and abundance variations correlate to layering in LDG. Orientation analysis of {112} twin systematics in cristobalite by EBSD confirms that cores were formerly single ß-cristobalite crystals. Combined with published experimental data, these results provide evidence for high-temperature (>1350 °C) magmatic crystallization of oscillatory zoned ß-cristobalite in LDG. Dendritic rims suggest growth across the glass transition by devitrification driven by undercooling, with transformation to α-cristobalite at low-temperature. This result represents the highest formation temperature estimate for naturally occurring cristobalite, which is attributed to the near pure silica composition of LDG and anomalously high temperatures generated during melting by meteorite impact processes.

Keywords: Cristobalite; silica; Libyan Desert Glass; EBSD; meteorite impact

INTRODUCTION

The high-temperature silica polymorph ß-cristobalite is thermodynamically stable from 1470-1726 °C; however, it is metastable at lower temperatures (Swamy et al., 1994; Heaney, 1994). The low-temperature polymorph α-cristobalite forms through displacive transformation below ~270 °C (Dollase, 1965), and is thus the only form of cristobalite found in natural samples (cf. Keith and Muffler, 1978; Damby et al., 2014). Occurrences of α-cristobalite (hereafter simply cristobalite) are restricted to volcanic glass (e.g., Swanson, 1989; Watkins et al., 2009), volcanic ash and/or soils (Horwell et al., 2013), hydrothermal/diagenetic deposits (Dollase, 1965; Shoval et al., 1997), and granulite facies rocks (Darling et al., 1997). The only other significant terrestrial occurrences of cristobalite are in high-temperature melt rocks, including those formed during meteorite impact (e.g., Ferrière et al., 2009; Trepmann et al., 2020), and less commonly, fulgurite (e.g., Crespo et al., 2009). Extra-terrestrial occurrences of cristobalite include lunar basalts (e.g., Christie et al., 1971), Martian rocks, including shergottites (Leroux and Cordier, 2006) and nakhlites (Kuebler, 2013), and diogenite meteorites (Benzerara et al., 2002). Here we describe a study to test formation hypotheses for cristobalite in Libyan Desert Glass (LDG).

Occurrences of LDG are found over several thousand km^2 in western Egypt. It consists of high-silica glass formed by fusion of a quartz-rich source, widely attributed to meteorite impact (e.g., Koeberl, 1997; 2000; Koeberl and Ferrière, 2019; Cavosie and Koeberl, 2019; Svetsov et al., 2020). The LDG is yellow to green and translucent, although some pieces are dark and others milky. In hand-sample, LDG can be nearly featureless; however, some samples have irregular white and/or brown layers. Cathodoluminescence and trace element studies show LDG is pervasively layered at ~10 μm-scale (e.g., Gucsik et al., 2004; Greshake et al., 2010), and some dark layers have a meteoritic geochemical signature (e.g., Koeberl, 2000).

Cristobalite in LDG has been documented in optical images (Spencer, 1939; Kleinmann, 1969; Greshake et al., 2010; Swaenen et al., 2010; Fröhlich et al., 2013), and its composition determined by electron microscopy (Greshake et al., 2010, 2018). Identification of α-cristobalite was confirmed using Raman spectroscopy (Greshake et al., 2010; Swaenen et al., 2010; Aramendia et al., 2011) and Fourier transform infrared spectroscopy (Fröhlich et al., 2013). Electron microprobe studies show LDG cristobalite is nearly pure silica (mostly >98 wt% SiO_2); Al is the second most abundant element (Al_2O_3 = 0.2 to 1.1 wt%), followed by Fe and Ti (Barnes and Underwood, 1976; Greshake et al., 2010, 2018). The LDG also contains little water (1100-1500 ppm, Frischat et al., 1984; Beran and Koeberl, 1997). Evidence of possible twinning in LDG cristobalite includes lamellar features in transmitted light images (Barnes and Underwood, 1976; Greshake et al., 2010). A transmission electron microscopy (TEM) study reported sub-μm mullite inclusions in LDG cristobalite (Greshake et al., 2018).

The round shape of LDG cristobalite (e.g., Spencer, 1939) and alignment within layers in some samples, have been cited as evidence that LDG cristobalite formed by devitrification (e.g., Barnes and Underwood, 1976; Seebaugh et al., 1985). In contrast, others have interpreted a magmatic origin for LDG cristobalite, citing its high temperature stability, and twinning as evidence of former ß-cristobalite (e.g., Greshake et al., 2010; 2018). Conclusive evidence to support either hypothesis remains elusive.

MATERIALS AND METHODS

The seven studied LDG samples are from western Egypt, and include characteristics previously described, such as locally containing optically dark and/or light-colored layering (see Online Materials for additional details). Samples were imaged and analyzed for orientation by scanning electron microscopy (SEM) using a Tescan Mira3 FE-SEM in the John de Laeter

Centre (JdLC) at Curtin University. Images include secondary electron (SE), backscattered electron (BSE), and panchromatic cathodoluminescence (CL) images. Acquisition of orientation data for cristobalite by electron backscatter diffraction (EBSD) used similar protocols for silicate minerals (e.g., Cavosie et al., 2018a). Orientation data were collected with an Oxford NordlysNano EBSD detector and Oxford Instruments AZtec software program (v. 3.3). The LDG cristobalite grains yielded high-quality diffraction patterns (average mean angular deviation values <0.5°). The EBSD map was collected with a step size of 200 nm, which yielded 2.4 M points. Figures showing pattern quality (band contrast, BC), orientation (inverse pole figure, IPF) and stereonets were plotted using the Tango and Mambo modules in the Oxford Instruments/HKL Channel5 software program (v. 5.12). Energy dispersive spectroscopy (EDS) elemental abundances were not calibrated.

Analysis of LDG and cristobalite by electron microprobe analyser (EMPA) was conducted using a JEOL JXA-8530F field emission microscope with Probe For EMPA acquisition software at the Centre for Microscopy, Characterization and Analysis at the University of Western Australia. Operating conditions included a 15 kV accelerating voltage, 15 nA current, and a 10 μm defocused beam; analyses were spaced at least 25 μm apart. A combination of glass and mineral standards were employed; Smithsonian Institution basaltic glass (NMNH111240-52 VG2) was analyzed to estimate precision. Calculated error based on nine analyses of basaltic glass are 0.1 rel% (Ti), 1-3 rel% (Si, Ca, Mg, Mn, Na, Fe), and 6-8 rel% (Al, K, P). Elements are expressed as molecular oxides (Tables 1 and 2). The EMPA data are available in Table 1 (LDG), Table 2 (cristobalite) and Online Materials (Tables OM1 and OM2).

Analysis of LDG and cristobalite by laser ablation inductively coupled plasma mass spectrometry (LAICPMS) was accomplished using a RESOlution M-50A-LR incorporating a

Compex 102 excimer laser, coupled to an Agilent 8900 QQQ ICP-MS at the GeoHistory Facility, JdLC, Curtin University. Analyses with a 50 μm spot size were spaced at least 10 μm apart. Glass standard NIST 612 was used as the primary reference material to calculate elemental concentrations (using stoichiometric ^{29}Si as the internal standard element with an EMPA-determined Si content for LDG of 46.34 wt.% Si) and to correct for drift. Reproducibility of secondary standard glass analyses yielded an accuracy of between 0.5 and 5 rel%. Data were collected for 37 elementals; abundances (in ppm) are presented in Tables 3 (LDG), Table 4 (cristobalite), and Online Materials (Tables OM3 and OM4).

Time-of-flight secondary ion mass spectrometry (ToF-SIMS) maps of Al distribution were collected using a Tescan Lyra3 focused ion beam scanning electron microscope (FIB-SEM) fitted with a Tofwerks compact ToF-SIMS detector located in the JdLC at Curtin University. Data were collected using a monoisotopic ^{69}Ga primary ion source operated with an accelerating voltage of 30 kV and a beam current of 300 pA, resulting in a nominal lateral resolution of ≤100 nm. ToF-SIMS maps and spectra were collected by scanning 15 x 15 μm areas (effective pixel size ~ 60 nm) for 20 frames. The 2D elemental maps showing Al distribution were extracted from the volume analyzed using the Tofwerk's ToF-SIMS Explorer software (v. 1.3.); Al abundances were not calibrated.

RESULTS

General observations of LDG

The LDG samples analyzed in this study are light yellow, translucent, and contain optically visible layering. All samples are pervasively layered in CL images and EDS maps down to the ~10 μm scale (Figs. 1-3), similar to that shown previously (Gucsik et al., 2004). Layering in LDG documented in this study at the 10s to 100s of micrometer scale (CL, BSE, and

EDS images) is distinguished from previously reported optically discernible layering in LDG at the mm scale (e.g., Greshake et al., 2010); the microscopic layering reported here is likely a manifestation of the macroscopic layering, but a rigorous correlation was not attempted. Layers observed here vary in thickness, extend laterally for several mm, and range from broadly linear to highly contorted (Fig. 1A). In general, layering in LDG and cristobalite is best resolved in CL images; herein, we refer to 'CL light' and 'CL dark' layers.

Cristobalite is readily discernible in CL images of LDG (Fig. 1B); grains in this study range from round to oval-shaped, with most 0.25 to 0.5 mm in diameter. All cristobalite grains observed (approximately 25) are zoned in CL, with distinct cores and rims (Fig. 2). Rims are generally about ~50 μm wide, and uniformly brighter in CL than cores. The CL dark cores have geometric shapes, with some nearly hexagonal (Fig. 2A-C). Linear features that are dark in CL radiate from the center of cores in some grains and terminate at the core-rim boundary (Fig. 2A,C). Other features include narrow enveloping layers with dark CL emission along grain boundaries (Fig. 2C) and cracks (Fig. 2B). The hexagonal shapes and linear features in LDG cristobalite (Fig. 2A-C) bear a striking resemblance to experimentally nucleated euhedral ß-cristobalite grains in vitreous silica (Fig. 2D) (Wagstaff, 1968). Eleven cristobalite grains from three samples of LDG were analyzed by EBSD, and all have core-rim microstructures. A grain from sample LDG-2018-4 (hereafter grain L4) was chosen as a representative example of LDG cristobalite for detailed analysis based on the presence of a well-developed core-rim microstructure.

Analysis of cristobalite grain L4 and surrounding LDG

Secondary and backscattered electron imaging (SE, BSE). Grain L4 is round, approximately ~250 μm across, and contains a network of fractures (Fig. 3A). All fractures

160 truncate other fractures; none traverse the entire grain, nor do they extend into LDG (Fig. 3A).
161 Subtle BSE contrast variation in the center of the grain suggests the presence of a core-rim
162 microstructure (Fig. 3B).

163 **Cathodoluminescence (CL) imaging.** A distinct core-rim microstructure is visible in
164 CL, with the boundary delineated by a narrow CL light feature, and the core darker than the rim
165 (Fig. 3C). The upper two-thirds of grain L4 is in a CL light layer, and the lower one-third of the
166 grain is in a CL dark layer (Fig. 3C). Superimposed on the broad CL layering are discrete light
167 and dark wispy layers at the ~10 μm scale that can be traced uninterrupted across the glass-rim
168 boundary (Fig. 3C, top left). The cristobalite rim has a conspicuous internal web-like structure,
169 defined by a network of irregular ~5 μm shapes with CL light boundaries. In contrast, the core
170 consists of broad areas of overall subdued CL intensity. There are also discrete, linear, CL light
171 features in the core, some of which are sub-parallel to the core-rim boundary. Subtle evidence of
172 LDG layering is locally observed in the core.

173 **Energy dispersive spectroscopy (EDS).** Elements detected by EDS include Si, O, Al,
174 Fe, and Ti; however, only Al displays resolvable spatial distribution variations (Fig. 3D). In
175 general, areas of relatively high Al abundance (bright) are dark in CL, whereas areas of relatively
176 low Al abundance (dark) are light in CL (Fig. 3C,D). As in the CL image, discrete ~10 μm wide
177 Al-rich and Al-poor layers in the glass are visible as uninterrupted features across the rim of
178 grain L4 (Fig. 3D, top left). In contrast to the glass-rim boundary, Al layering is largely truncated
179 at the core-rim boundary. In the core, vestiges of the broad Al layering are visible; however, the
180 most prominent features are concentric and continuous zones ~ 5 μm wide characterized by
181 alternating layers of relatively high Al abundance (bright) and relatively low Al abundance

(dark) that are discordant to layering. The Al zoning pattern in the core forms a rectangular shape with accentuated corners that resembles a crystalline form (Fig. 3D).

Electron backscatter diffraction (EBSD). Orientation data show that grain L4 exhibits a distinct ~150 μm diameter core and ~50 μm wide rim with a well-defined boundary (Fig. 4A). Fractures are not concentrated in either the core or rim, and do not seem to be influenced by the core-rim boundary (Fig. 4A). Fracture-bound subgrains are essentially undeformed (<1° of internal misorientation), and the same orientation domains across fractures are misoriented by <1°. No evidence of crystal-plastic deformation or significant rigid block rotation by fracturing was detected.

Both core and rim of grain L4 are pervasively twinned. The core consists of two regions, each defined by three sets of intergrown twins (Fig. 4B, labelled 1-3, and 4-6). In each core region, one twin orientation is prevalent (i.e., 2 and 4), and hosts the other two twins. Boundaries between twin domains are straight and terminate at fractures (Fig. 4B). Each set of intergrown twins is related by a systematic misorientation of 90°/<110> (Fig. 4C,D). The misorientation relation results in shared directions for several crystallographic axes, including [001] and [110], [110], [100] and [112], and [112] (Fig. 4C,D). The two twin regions in the core (1-3 and 4-6) also share crystallographic directions, including [100] and [112] (Fig. 4C,D). Analysis of orientation data on stereonets, in conjunction with geometry of twin boundaries, confirms the presence of six discrete {112} twin orientations in each core region (labelled a-f in Fig. 5A-C). The boundary between the core regions (Fig. 5D) is defined by a 70°/<100> misorientation relation, which identifies it as a shared {011} twin plane (Fig. 5E). Twin orientations in the rim include both {112} and {011}, similar to the core. A notable feature in the rim are elongate

204 dendritic twin domains that are orientated orthogonal to the core-rim boundary (Fig. 5F).
205 Individual twins in the rim can be traced across fractures.

206 **Time-of-flight secondary ion mass spectrometry (ToF-SIMS).** Fine-scale Al
207 distribution in grain L4 was further investigated using ToF-SIMS mapping. The spatial
208 distribution of other elements, including Si and O, was homogenous in mapped areas, apart from
209 regions of high Al. Six 15 x 15 μm maps of Al distribution were made in the rim (n=1), the rim-
210 core boundary (n=3), and in the core (n=2); these areas were chosen to evaluate if features
211 visible in CL, EDS, and orientations maps are correlated (Fig. 6A, E). The ToF-SIMS maps
212 reveal two types of Al distribution. In the rim (Fig. 6B), Al forms a discrete network of irregular
213 shapes, each ~5 μm across, similar to the network of bright features visible in CL (6A).
214 Comparison with orientation data shows that the ToF-SIMS Al map correlates to boundaries of
215 ~5 μm-sized cristobalite grains in the rim (Fig. 6A, IPFz). The width of Al-enriched regions is
216 approximately 0.2 μm. In contrast, ToF-SIMS Al maps in the core show linear features (Fig. 6C)
217 and/or discrete Al-rich spots 0.1-1.0 μm across, some of which form arrays (Fig. 6D). Linear
218 features defined by Al in the core correlate to bright features visible in BSE, CL, and EDS Al
219 maps, and are not coincident with grain boundaries (Fig. 6A,C-D). The spatial distribution of
220 discrete Al hot-spots in the core (Fig. 6C,D) appears to correlate to both sub-vertical (Fig. 6A,C)
221 and sub-horizontal (Fig. 6A,D) bands in the EDS Al map that form part of the oscillatory zoning
222 pattern (Fig. 3D).

223 The ToF-SIMS maps of the core-rim boundary (Fig. 6E-H) reveal the presence of
224 elongate, ~5 μm wide shapes up to ~10 μm long, defined by curved, semicontinuous high Al
225 lines both normal (Fig. 6F) and sub-parallel (Fig. 6G,H) to the core-rim boundary. The Al
226 abundance inside the elongate shapes is comparatively low and homogeneous, in contrast to

227 adjacent rim domains, which consist of high Al networks similar to those described above (Fig.
228 6B). The high Al boundaries are partially resolved in the EDS-Al map (Fig. 6E-EDS), which
229 suggests the features are part of oscillatory growth bands.

230 **Major and minor element analysis (EMPA).** Thirty EMPA analyses on sample LDG-
231 2018-4 include 21 on glass (Table 1) and 9 on cristobalite grain L4 (Table 2). Of 12 elements
232 analyzed, only Si, Al, Fe, and Ti are at detectable levels in all analyses; other elements are
233 variably or entirely below detection. Analytical totals for glass (98.6-101.1 wt.%) and cristobalite
234 grain L4 (99.7-101.1 wt.%) indicate all major and minor elements were measured. Silica
235 variations in LDG and cristobalite correlate to CL intensity (Fig. 7A,B); CL dark layers have
236 approximately ~1 wt% lower silica values (average = 97.8 wt% SiO_2), whereas CL light layers
237 are nearly pure silica (average = 99.1 wt% SiO_2). In CL dark layers, abundances of other
238 elements are elevated, including Al_2O_3 (average = 1.33 wt%), FeO (average = 0.22 wt%), and
239 TiO_2 (average = 0.14 wt%).

240 Nine EMPA analyses of cristobalite grain L4 include four spots in the core and five spots
241 in the rim, and provide values averaged over the 10 μm beam diameter (Fig. 8A). Among all spot
242 analyses on cristobalite, average values for SiO_2, Al_2O_3, FeO, and TiO_2 in both domains (Fig.
243 8B; Table 2) are similar to average values of LDG (Table 1). However, when EMPA analyses
244 are grouped by CL intensity (e.g., CL dark cores and rims vs. CL light cores and rims) (Fig. 8B.
245 lower panel), a bimodal population emerges, with CL dark domains yielding higher Al_2O_3 values
246 (average = 1.71 wt% Al_2O_3) than values from CL light domains, (average = 0.50 wt% Al_2O_3)
247 (Table 2). Values for FeO and TiO_2 follow similar trends, with higher values in CL dark areas
248 and lower values in CL light areas. In general, minor element abundances in cristobalite are
249 similar to cristobalite in other LDG samples (Greshake et al., 2010, 2018) (Fig. 8B, lower panel).

Trace element analysis (LAICPMS). Forty-five LAICPMS spot analyses, each 50-µm-diameter, were made , including 25 on glass (Table 3) and 20 on cristobalite grain L4 (Table 4). Ten analyses (spots 1-10) were done in a 0.9 mm linear transect across layers that contain grain L4, with a close spatial relationship to EMPA analyses (e.g., Fig. 7B). The other 15 analyses were in random spots near grain L4. Abundance patterns for most elements in LDG correlate to CL intensity, with higher abundances in CL dark layers and lower abundances in CL light layers (Fig. 7B,C). Abundances of 37 elements in LDG indicate three are present at >1000 ppm (Al, Fe, Ti), two at 100-1000 ppm (K, Zr), seven at 10-100 ppm (Na, Mg, Ca, Sr, Ba, La, Ce), 19 at 1-10 ppm (Li, B, Sc, V, Cr, Mn, Cu, Zn, Y, Nb, Hf, Pb, Th, U, Nd, Pr, Sm, Gd, Dy), and six <1 ppm (Co, Ni, Rb, Eu, Er, Yb). Element abundances in LDG and cristobalite grain L4 are similar; both materials are variably depleted relative to upper continental crust (Fig. 9A). The most depleted elements include Na, Mg, K, Ca, and Rb; the least depleted include B, Zr, and Hf. Several elements are enriched in cristobalite over LDG, including Co, Ni, and Cu.

The largest variation in element abundance, for both LDG and cristobalite, occurs between CL dark and CL light layers (e.g., Fig. 8A). Total minor/trace element abundance varies by nearly a factor of two between CL light layers (average = 6300 ppm) and CL dark layers (average = 11,700 ppm) (Table 3). A similar a range occurs between CL light layers in cristobalite (average = 6705 ppm) and CL dark layers (average = 13,758 ppm) (Fig. 8A; Table 4). Covariations of Al and Fe correlate to CL intensity, rather than domain (i.e., core vs. rim). Average values for Al_2O_3 from LAICPMS analyses agree well with those derived by EMPA for cristobalite grain L4 for both CL dark layers (1.7±0.23 wt.%, 1σ, EMPA vs. 1.90±0.21 wt.%, 1σ, LAICPMS) and CL light layers (0.5±0.09 wt.%, 1σ, EMPA vs. 0.77±0.18 wt.%, 1σ, LAICPMS). No evidence of core-rim geochemical zonation was detected (Fig. 8C).

Inclusions in cristobalite. The oscillatory zoning pattern defined by Al in the core of grain L4 (Fig. 3D, 6C,D) was further investigated. Close inspection with BSE imaging revealed that the ~1 μm Al 'hot spots' visible in the core by EDS and ToF-SIMS (Fig. 10A) consist of parallel arrays of aligned inclusions (Fig. 10B). The arrays are sub-parallel to the core-rim boundary (Fig. 4A), and cross-cut twins. Inclusions are up to ~500 nm across, and most appear polyphase (Fig. 10B,C). The inclusions are Al-rich as measured by EDS (Fig. 10D). Attempts to identify the inclusions using a 20 nm EBSD spot size were unsuccessful; this may be due to recessed surfaces from preferential polishing, lack of crystallinity, or other effect. Mullite inclusions were previously reported in LDG cristobalite (Greshake et al., 2018); inclusions identified here are tentatively interpreted as mullite, although confirmation requires further study. Both EMPA and LAICPMS spot analyses may have incorporated some of these inclusions.

DISCUSSION

Aspects of LDG formation

Duration and temperature of melting. Given that impact-induced melting is the most widely favored mechanism for generation of LDG, quartz in the precursor would have been rapidly superheated above its melting temperature. Numerical modelling of near-surface radiative heat transfer generated by different impact scenarios suggests melting lasted from 1 to 7 minutes, producing a layer up to 10 cm thick, which solidified after 8 minutes (Svetsov et al., 2020). Earlier models featured LDG forming a >1 m thick sheet (e.g., Seebaugh et al., 1985).

The Svetsov et al. (2020) model features silica melting at ~2025 °C, whereas at equilibrium, silica melting occurs at 1726 °C (Swamy et al. 1994). Experiments involving rapid superheating of quartz show that silica melt can form at 1550 °C (Ainslie et al., 1961); melting of

the LDG precursor could thus have begun by ~1550 °C (e.g., Greshake et al., 2010). Mineral-based observations support the idea that the LDG precursor experienced temperatures in excess of 1550 °C (Fig. 11). The presence of Al-rich orthopyroxene melt by ~1550 °C (Greshake et al., 2010), decomposition of kaolinite by 1600 °C (Greshake et al., 2018), zircon dissociation by 1675 °C (Kleinmann, 1969; Cavosie and Koeberl, 2019), and rutile melting by ~1800 °C (Greshake et al., 2018) are consistent with modelled temperatures >2000 °C (Svetsov et al., 2020), which implies at least ~300 °C of superheating above the silica liquidus.

Porosity and layering in LDG. Dilation studies show LDG has a relatively open structure, with thermal and compositional characteristics similar to Type III silica glass (Brückner, 1970; Frischat et al., 1984, 1989). The LDG glass no effective porosity, other than bubbles in some samples (e.g., Seebaugh et al., 1985). Annealing experiments on silica glass powder (5-25 μm spheres) found no reduction in porosity from 1200 to 1350 °C; however, above 1550 C°, the spheres sintered into non-porous glass in 5 to 10 minutes (Breneman and Halloran, 2014). This observation may have significance on minimum temperature and heating duration if the source was porous (e.g., Sighinolfi et al., 2020). The LDG contains ubiquitous layering visible in CL and element distribution maps (Gucsik et al., 2004, Greshake et al., 2010; this study); the layering likely reflects mineralogical heterogeneity of the precursor. The observation that LDG layering is incorporated within cristobalite crystals (Fig. 3) establishes that cristobalite formed after the layering.

LDG glass transition. As a nearly pure silica superheated melt in contact with atmosphere, LDG would have experienced rapid supercooling, producing a highly viscous state. The glass transition temperature (T_g) is the temperature at which supercooled melt and glass are in metastable equilibrium (e.g., Richet et al., 1982); the structural state of a supercooled melt is

locked in at T_g. Devitrification of LDG would have occurred if melt temperature was held at or above T_g during cooling; however, TEM analysis found no evidence of devitrification (Pratesi et al., 2002). Below T_g, increased viscosity would have prohibited element mobility and crystallization. Estimates of T_g for synthetic silica glass range from 1000 °C to 1200 °C, the latter for densified glass (Brückner, 1970). For LDG, estimates for T_g of ~1200 °C have been proposed (fictive temperature, Frischat et al., 1984). However, T_g is a function of cooling rate; rapidly supercooled silica has a higher T_g than slowly cooled silica (Brückner, 1970; Moynihan, 1974). For vitreous silica, values for T_g of 1207 °C (slow cooling) and 1327 °C (rapid cooling) have been experimentally determined (Richet et al., 1982). Determining which T_g value is appropriate for LDG (Fig. 11) from the range of estimates (1000 to ~1325 °C) depends on the cooling rate assumed.

Evidence for β-cristobalite in LDG

Twinning and phase heritage analysis. Detecting the former presence of ß-cristobalite in LDG is achievable through analysis of twin orientation relations in α-cristobalite by applying a concept known as 'phase heritage' (Timms et al., 2017a). The basis of phase heritage analysis is that systematic crystallographic orientation relations among co-existing domains of a given phase (e.g., twins or neoblasts) are only established through transformation of a former polymorph that typically is no longer present (Cayron et al., 2006). The concept of phase heritage analysis has been applied in TEM studies (e.g., Nord, 1992, 1994; Kerschhofer et al., 2000; Lussier et al., 2017), and more recently, using EBSD. EBSD-based phase heritage applications have provided evidence for the former existence of high-pressure and/or temperature phases for zirconia (Humbert et al., 2010; Timms et al., 2017a,b; White et al., 2018),

341 zircon (e.g., Cavosie et al., 2016, 2018a,b; Erickson et al., 2017), monazite (Erickson et al.,
342 2019), and Ti-bearing phases (Pearce and Escolme, 2021).

343 Twinning in cristobalite results from loss of symmetry during the ß (cubic) to α
344 (tetragonal) transformation, which changes the space group ($Fd\bar{3}m \rightarrow P4_32_12$), point group
345 ($m\bar{3}m \rightarrow 422$), and lattice ($cF \rightarrow tP$) (Nord, 1992). Up to 12 twin domains may form during the ß-α
346 transformation (Hatch and Gosse, 1991). The most common, termed pseudomerohedral twins by
347 Nord (1992, 1994), result from loss of the 3-fold rotation axis. Other twins result from loss of
348 center of symmetry (merohedral) and translational symmetry (antiphase domains) (Nord, 1992).
349 Studies using TEM have reported twin orientations of {112}, {200}, {011}, and {012} in α-
350 cristobalite (e.g., Christie et al., 1971; Withers et al., 1989). In addition, an EBSD study of
351 dendritic cristobalite reported {111} twins (Zhao et al., 2008).

352 Analysis of orientation data in LDG cristobalite, combined with geometric arguments,
353 allowed confirmation of the dominant twin orientation as {112} (e.g., Withers et al., 1989), with
354 each twin defined by a systematic 90°/<110> misorientation relationship (Dollase, 1965). We
355 identified {112} pole clusters corresponding to the orientation of the trace for each twin (Fig. 5),
356 as they intersect lines orthogonal to the trace; pole clusters for {111} (Zhao et al., 2008), were
357 found to be systematically offset from the predicted twin plane by ~5°. In LDG cristobalite, the
358 presence of six {112} twins in each core domain (Fig. 5) match that predicted to form during
359 transformation from ß- to α-cristobalite (Nord, 1992), and is consistent with the core originally
360 consisting of either a single twinned ß-cristobalite crystal, or two intergrown crystals, one
361 represented by domains 1-3, and the second by domains 4-6.

362 Coincidence of crystallographic directions in each core twin domain (Figs. 4, 5) (e.g.,
363 domains 1-3 and 4-6) follows the predicted orientation of crystallographic axes resulting from

the ß-α transformation (Fig. 12). A single cubic ß-cristobalite crystal will produce 3 tetragonal α-cristobalite variants (Withers et al., 1989). The c-axis and [110] direction of each tetragonal variant are orthogonal, resulting in shared orientations for [001] and {110}, {110}, {100} and {112}, and {112} (Fig. 4c). These observations support orientation relationships of <001>β = <001>α, <001>β = <110>α, and <110>β = <110>α. Alignment of three orthogonal <001> directions of the tetragonal phase (Figs. 4, 5) with <001> of the cubic parent is analogous to that described for the cubic to tetragonal transformation of zirconia (Timms et al., 2017b).

Oscillatory growth zoning. Distribution of Al in cristobalite cores defines an oscillatory pattern resembling growth zoning in igneous minerals that crystallize from melt. The Al distribution pattern in the core of grain L4 consists of multiple concentric and generally continuous layers of variable thickness that oscillate in relative Al abundance and preserve a crystalline form (Figs. 3D, 6A,E). Our investigation of the oscillatory pattern in a region of high Al abundance (Fig. 10) demonstrated that Al 'hot spots' in EDS and ToF-SIMS maps are arrays of <500 nm sized Al-rich inclusions. Inclusion arrays in the core do not correlate to twin planes (Fig. 10B), but are parallel to the well-defined nearby core-rim boundary (Fig. 4A). The Al-rich inclusions are thus interpreted to have been incorporated during growth of ß-cristobalite. Elsewhere in the core, elongate patterns of Al enrichment defined by continuous curvilinear bands visible in ToF-SIMS maps (Fig. 6F-H) appear to represent crystal edges or interfaces where Al was rejected during growth (e.g., Watkins et al., 2009).

Diffusion of Al in nearly pure silica (quartz and amorphous) at high temperature (~1000 °C) is slow (10^{-24} to 10^{-22} m^2s^{-1}, Francois-Saint-Cyr et al., 2003; Schipper et al., 2020); Al is also assumed to diffuse slowly in cristobalite. Studies of trace element incorporation in magmatic crystals describe processes that can enrich trace elements along planar growth interfaces

This is the peer-reviewed, final accepted version for American Mineralogist, published by the Mineralogical Society of America.
The published version is subject to change. Cite as Authors (Year) Title. American Mineralogist, in press.
DOI: https://doi.org/10.2138/am-2021-7922. http://www.minsocam.org/

(Hammer, 2008). One is a diffusive boundary layer processes, whereby slowly diffusing incompatible elements become enriched along the melt-crystal interface due to crystal growth rates exceeding rates at which incompatible elements diffuse away into the melt; when the enriched layer is incorporated into the crystal under local equilibrium conditions, the resulting abundance is beyond that predicted for equilibrium partitioning based on the bulk composition (Milman-Barris et al., 2008). Another process is solute trapping, which happens when rapidly growing crystals incorporate melt inclusions dominated by the incompatible element(s). In this process, observed element enrichment is also not representative of abundance in the bulk material (Milman-Barris et al., 2008). Solute trapping can be caused by high growth rates during large supercooling, and also during interface-controlled growth (Hammer, 2008).

The Al-rich inclusions documented here (Fig. 10) are preferentially concentrated in areas corresponding to high Al abundance layers in LDG (Fig. 3D), whereas discrete, continuous linear Al enrichments occur outside of high Al abundance layers (Fig. 6). The oscillatory zoning pattern thus appears to record local redistribution of Al by diffusive boundary processes at the crystallization front in low Al abundance layers, whereas solute trapping of Al-rich inclusions occurred in high Al abundance layers. Both processes are viewed as manifestations of disequilibrium partitioning resulting from rapid growth of cristobalite in heterogeneously layered silica melt.

Considerations for β-cristobalite growth in LDG

Factors governing crystallization. Important factors controlling crystallization of silicate melts include (1) reactions at the crystal-melt interface, (2) stability of the planar interface, (3) element diffusivity at the interface, (4) removal of latent heat, and (5) flow of bulk material (convection) (Kirkpatrick, 1975, 1981; Hammer, 2008). In the case of LDG cristobalite,

which is compositionally nearly identical to LDG, diffusivity of silica was not rate-limiting, but diffusivity of minor elements such as Al would have influenced their incorporation into cristobalite. Convective heat flow or flow of bulk material are unlikely to have occurred in the thin (up to 10 cm) modelled thickness of LDG (e.g., Svetsov et al., 2020).

Former β-cristobalite grains in LDG are viewed as either having crystallized as magmatic grains in static melt when LDG was a viscous silica liquid, or alternatively, are a product of devitrification after LDG solidified but resided at a temperature above T_g. At temperatures below T_g, melt would not be present, viscosity would have inhibited element mobility, and crystallization of cristobalite with oscillatory growth zoning would not have been possible. Below we discuss observational and experimental data to evaluate processes that may have affected crystallization of cristobalite in LDG.

Grain morphology, growth mechanisms, effects of supercooling. Cores of LDG cristobalite are interpreted to have formed as euhedral β-cristobalite crystals with planar boundaries (Fig. 4A). Such characteristics are typical of interface-controlled growth, which occurs at high-temperature (near liquidus) with low degrees of supercooling, where diffusivity is high and growth rate is low (Kirkpatrick, 1975, 1981; Jambon et al., 1992; Hammer 2008). In contrast, rims consist of dendritic grains (Fig. 5F); dendrites are typical of diffusion-controlled growth at high degrees of supercooling where growth rate is high (Christensen et al., 1973; Kirkpatrick, 1975; Jambon et al., 1992). Individual grains in the rim range from 5-10 μm, with discrete twinned domains up to ~50 μm long that radiate orthogonally from the core (Fig. 5F). The boundary between the core and rim is discrete rather than gradational (Fig. 4A), indicating the rim formed as an epitaxial overgrowth.

The core-rim microstructure of LDG cristobalite records a two-stage growth history. However, it is possible that increased supercooling alone may have triggered an instability of the initial planar interface, leading to precipitation of dendritic rims (Jackson, 1967; Kirkpatrick, 1975). The physical process(es) that drove the change in supercooling regime for LDG is not known, such as whether it was a gradual or abrupt process, and whether it was triggered by factors external (e.g., environmental) or internal (e.g., interface effects) to LDG. Distinctive cristobalite core-rim microstructures are evident in published images (e.g., Spencer, 1939; Greshake et al., 2010; Fröhlich et al., 2013), indicating the petrogenetic conditions described here occurred throughout the LDG field. The sequence of interface-controlled core growth followed by dendritic rim growth for LDG cristobalite is opposite to descriptions of oscillatory P zoning in olivine, whereby crystallization of dendrites by diffusion-controlled growth transitions to interface-controlled growth (Welsch et al., 2014; Watson et al., 2015). The contrasting growth processes between LDG cristobalite and magmatic olivine may reflect differences in degree of superheating, duration at high temperature, degree of supercooling, or other factors.

The crystalline form defined by Al growth zoning in the core of grain L4 merits further mention. The Al distribution pattern on the polished surface is a four-sided intersection of a polyhedron with conspicuously ‘stretched’ corners and concave sides (Fig. 3D). The morphology of cubic crystals grown by surface nucleation-controlled growth at relatively large undercooling has been described in the context of a surrounding three-dimensional diffusion field, supersaturation, and interface growth kinetics in a static (non-convecting) melt (Kuroda et al., 1977; Kirkpatrick, 1981). Growth of cubic crystals under these conditions preferentially occurs at corners or edges, relative to faces, resulting in the interface ‘sloping down’ away from corners, and towards face centers. Diagrams of such crystals in Kuroda et al. (1977) and Kirkpatrick

455 (1981) with 'stretched' corners and concave sides look remarkably similar to the form defined by
456 Al in the core of cristobalite grain L4 (Fig. 3D). These studies provide cogent descriptions of a
457 kinetic process that explains the morphology of growth zoning in cores of LDG cristobalite, and
458 are in agreement with our interpretation of interface-controlled growth.

459 **Nucleation of cristobalite in LDG.** Observational data support formation of β-
460 cristobalite in LDG by internal (homogeneous) nucleation, including: (1) all cristobalite
461 occurrences reported since Spencer (1939) are internal to LDG; we are not aware of occurrences
462 on free surfaces; (2) there is little to no porosity in LDG; bubbles (e.g., Seebaugh et al., 1985),
463 are not ubiquitously associated with cristobalite (c.f., Kleinmann, 1969); (3) layering in LDG is
464 incorporated within cristobalite grains; (4) the extent of fusion indicates remnant quartz grains
465 from the precursor are unlikely nucleation sites; no 'seed' crystals or other objects have been
466 observed in cores of cristobalite grains that record evidence of heterogeneous nucleation.

467 If rapidly heated to >2000 °C (Fig. 11), the LDG precursor would have experienced at
468 least 300 °C of superheating to superliquidus temperatures. Superheating, followed by rapid
469 supercooling, is known to depolymerize silicate melts (Hammer, 2008), and likely inhibited
470 extensive nucleation of cristobalite. In basaltic liquids, the magnitude of superheating, rather
471 than its duration, is the most significant effect on delayed nucleation (Kirkpatrick, 1981).
472 Further, if LDG was supercooled as a structurally unrelaxed melt (Frischat et al., 1984, 1989),
473 delayed nucleation may have driven supersaturation, resulting in accelerated cristobalite growth
474 (Hammer, 2008).

475 **Temperature of cristobalite crystallization.** The maximum temperature for cristobalite
476 crystallization is ~1726 °C (Swamy et al. 1994), however most silicate melts require some
477 degree of undercooling to trigger crystallization (e.g., Kirkpatrick, 1975, 1981). Coarse

478 cristobalite cores imply a relatively low degree of supercooling, compared to the dendritic rims.
479 The crystallization temperature of cristobalite may have been substantially below the liquidus
480 (i.e., Ainslie et al., 1961); it could have crystallized within the thermodynamic stability field
481 (1726 to 1470 °C), or metastably at lower temperature.

482 Of relevance to crystallization temperature of LDG cristobalite is the observation that
483 experimentally nucleated ß-cristobalite grains in vitreous silica from 1350-1620 °C (Wagstaff,
484 1968) had a near-hexagonal form (in 2D), a shape consistent with polished octahedra, and
485 further, that some contained linear features in a radial pattern (Fig. 2D). Both hexagonal-shaped
486 cores and linear radial features were observed in LDG cristobalite (e.g., Figs. 2, 3). The size of
487 the grain in Figure 2D is not given; however others from the same experiments are 200-500 μm
488 in diameter (Wagstaff, 1968), and thus comparable in size to those in LDG. The similar
489 morphological features of LDG cristobalite and experimentally nucleated ß-cristobalite provides
490 support for the possibility that cores of LDG cristobalite grains may have crystalized at >1350 °C
491 (Fig. 11).

492 **Cristobalite growth rate.** Experimentally-derived crystallization rates of cristobalite in
493 fused silica include surface (heterogeneous) nucleation rates and internal (homogeneous)
494 nucleation rates, typically measured over durations from hours to days; internal nucleation rates
495 for cristobalite (e.g., Wagstaff, 1968, 1969) are slower than surface nucleation rates (e.g., Ainslie
496 et al., 1961). Crystallization rates for internal nucleation of β-cristobalite in vitreous silica ranged
497 from 0.13 μm/minute at 1675 °C (Fig. 11) to 0.02 μm/minute at 1475 °C (Wagstaff, 1969).
498 These values overlap crystallization rates in siliceous melts (10^{-9} to 10^{-13} ms^{-}) summarized by
499 Watson et al. (2009). Using the fastest cristobalite crystallization rates from Wagstaff (1969),
500 formation of a 150 μm diameter grain would require 9.6 hours, which is far beyond the ~7

minute duration of liquid LDG suggested by modelling (Svetsov et al., 2020). In contrast, formation of a 150 μm diameter core within the modelled ~7 minute duration of liquid LDG would require a crystallization rate of ~20 μm/minute, two orders of magnitude faster than experimental constraints (Wagstaff, 1968, 1969). Latent heat release may have influenced growth rate of cristobalite in supercooled LDG. Rapidly grown crystals in supercooled melt can release heat faster than it diffuses away from the interface, resulting in increased heating along the interface, in a process known as recalescence. Recalescence has been described in silicate melts (Whittington et al., 2021), however its effects on LDG cristobalite growth has not been studied. The conditions under which LDG formed are extreme in terms of the degree of superheating, the short duration of melting, and the degree of supercooling (e.g., Macris et al., 2018), all of which could have delayed nucleation and driven supersaturation of cristobalite, which makes crystallization rate difficult to characterize.

Comparison with other occurrences

Igneous and volcanic rocks. Cristobalite is often described from obsidian (e.g., Swanson and Fenn, 1986), where a magmatic origin at temperatures <1000 °C is inferred (see McArthur et al., 1998). Cristobalite in Martian meteorite NWA 856, a basaltic shergottite, is interpreted to have formed below ~1000 °C (Leroux and Cordier, 2006). A melt phase origin has been inferred to explain cristobalite inclusions in garnet from granulite facies metagabbro (Darling et al., 1997). The cristobalite occurrences listed above represent metastable crystallization below <1000 °C, forming grains that do not share characteristics of LDG cristobalite.

Dendritic cristobalite in volcanic rocks is interpreted to form by devitrification (e.g., Kayama et al., 2009; Watkins et al., 2009), driven by significant undercooling (Lofgren et al., 1971; Swanson et al., 1989; McArthur et al., 1998). Vapor phase deposition (VPD) of

cristobalite occurs in volcanic rocks that contain cavities (Rogers, 1922; Horwell et al., 2013; Schipper et al., 2020) and in hydrothermal experiments (Grieg et al., 1936). However, VDP could not have played a role in formation of cristobalite in LDG, given the low water content (Frischat et al., 1984; Beran and Koeberl, 1997), zero effective porosity, and absence of cavities with cristobalite.

High-temperature melts. Ferrière et al. (2009) described two high temperature processes that form ß-cristobalite in impact melt rocks. The first involves a solid-state transformation of α-quartz to diaplectic glass, followed by crystallization of ß-cristobalite at high-temperature (>1000 °C). The second mechanism involves a solid-liquid transformation of α-quartz to lechatelierite at high-temperature (>1700 °C), from which ß-cristobalite crystallizes. The solid-liquid transformation of α-quartz to lechatelierite, followed by crystallization of ß-cristobalite (Ferrière et al., 2009) seems most applicable, as LDG experienced near-total fusion. Cristobalite has been reported in fulgurite (e.g., Crespo et al., 2009), however, a review of global occurrences indicates cristobalite is rare in fulgurite (Pasek and Pasek, 2018).

A model for the formation of cristobalite in LDG

Most studies favour LDG originating from melting associated with meteorite impact, although other mechanisms have been proposed (see Koeberl, 1997; Greshake et al., 2018). In the context of a high-temperature origin scenario, LDG cristobalite has been proposed to result from both magmatic processes (e.g., Greshake et al., 2018) and devitrification (e.g., Seebaugh et al., 1985). We view the weight of observations as compelling evidence for magmatic growth of LDG cristobalite cores; the origin of dendritic rims is less clear. Our model features a multi-stage growth history of LDG cristobalite to explain formation of large, euhedral, oscillatory zoned cores surrounded by dendritic rims (Fig. 13). The LDG source is constrained as a high-purity,

547 quartz-rich precursor (Fig. 13A); its nature (e.g., alluvium, eolian sand, sandstone, quartzite) has
548 been discussed elsewhere (e.g., Abate et al., 1999; Koeberl and Ferrière, 2019). Elemental
549 analyses in this study (Fig. 9A) show LDG is variably depleted relative to upper continental crust
550 (Taylor and McLennan, 1995), consistent with a mature, quartz-rich precursor. The composition
551 of LDG in this study (Fig. 9A) is similar to other occurrences (Fig. 9B) (Koeberl, 1997; Barrat et
552 al., 1997; Magna et al., 2011), demonstrating broad homogeneity of LDG. Less depleted
553 elements (Fig. 9A, arrows) may record accessory minerals in the precursor, including zircon (Zr,
554 Hf), rutile (Ti), chromite (Cr), tourmaline (B), aluminum silicate (Al), or possibly clay minerals
555 (Al, B).

556 The precursor was superheated by at least 300 °C and fused to a layered (Figs. 1-3,7;
557 Gucsik et al., 2004), nearly pure (~99 wt%) silica melt at high-temperature (Fig. 13B). The
558 presence of Al-bearing phases in the precursor, possibly kaolinite (Greshake et al., 2018) or
559 andalusite, created Al-rich and Al-poor layers (Fig. 3D; Greshake et al., 2010). The minimum
560 melt temperature of LDG (Fig. 11) is ~1550 °C (rapid quartz melting, Ainslie et al., 1960),
561 although actual melt temperature was likely hotter (Svetsov et al., 2020).

562 Numerical models suggest LDG existed as liquid for up to ~7 minutes (Svetsov et al.,
563 2020). In this time, euhedral crystals of β-cristobalite, with various types of growth zoning
564 defined by Al distribution, nucleated from the layered viscous melt in an interface-controlled
565 regime during modest supercooling (Fig. 13C). There are few constraints on β-cristobalite
566 crystallization temperature (Fig. 11); experimental results (Wagstaff, 1968) allow the possibility
567 that cristobalite crystallized from 1350-1650 °C. We cite ~1350 °C from Wagstaff (1968) as the
568 lowest temperature reported at which euhedral β-cristobalite crystals have been shown to
569 nucleate within vitreous silica as the best estimate for minimum temperature of β-cristobalite in

570 LDG (Fig. 13C), while acknowledging that ß-cristobalite can form metastably at lower
571 temperatures.

572 Increased supercooling triggered the transition to a diffusion-controlled growth regime,
573 resulting in crystallization of dendritic ß-cristobalite rims as epitaxial overgrowths (Fig. 13D)
574 (e.g., Kirkpatrick, 1975; McArthur et al., 1998). Rim growth is assumed to have occurred within
575 the glass transition, from 1000 to ~1325 °C (e.g., Richet et al., 1982). The absence of
576 devitrification features in LDG at atomic scale (Pratesi et al., 2002) indicates rapid quenching.

577 The ß- to α-cristobalite transformation at ~270 °C resulted in a 4% volume reduction
578 (Dollase, 1965), creating fractures in LDG cristobalite (Fig. 13E). The final microstructure to
579 form was twinning (Fig. 13F). Twins extend across fractures in the rim, but not in the core,
580 suggesting twins in the rim formed before development of the fracture network. Twins in the
581 core formed subsequently, and are pinned by the fractures. The fracture network and twins likely
582 formed nearly simultaneously, given both are a consequence of the ß-α transformation.

583 **IMPLICATIONS**

584 No other natural occurrence of cristobalite is comparable to that found in LDG, in terms
585 of host rock composition, growth zoning, and core-rim microstructure. Experimental data for ß-
586 cristobalite formation in vitreous silica represent reasonable analogues for cristobalite formation
587 in LDG, as both the kinetics (rapid melting) and composition (pure silica) appear applicable to
588 LDG. The model presented is consistent with a high-temperature impact origin of LDG (e.g.,
589 Kleinmann, 1969; Koeberl, 1997; Greshake et al., 2018; Koeberl and Ferrière, 2019; Cavosie and
590 Koeberl, 2019; Sighinolfi et al., 2020). Our study is the first to quantify a multi-stage growth
591 history involving ß-cristobalite from any environment. The cores of LDG cristobalite grains may

592 represent natural examples of liquidus growth of ß-cristobalite within its thermodynamic stability
593 field, although metastable growth <1470 °C cannot be fully ruled out.

594 We describe the first occurrence of oscillatory growth zoning in cristobalite, here
595 recorded by concentric variations in Al content. Oscillatory zoning is common in other minerals
596 (e.g., plagioclase, zircon), and its occurrence in LDG provides insight into incorporation of trace
597 elements in cristobalite at extreme temperatures (>1350 °C). Phase heritage analysis of twins in
598 LDG cristobalite using EBSD provided evidence that confirmed the former presence of ß-
599 cristobalite. Phase heritage analysis of zircon, monazite, and baddeleyite has identified former
600 polymorphs; our study shows that twinned cristobalite is also suitable for detecting polymorphs
601 that are no longer present.

602 **ACKNOWLEDGEMENTS**

603 Support was provided by the Space Science and Technology Centre, a Curtin Research
604 Fellowship, and the John de Laeter Centre at Curtin University. The GeoHistory laser ablation
605 Facility was enabled by AuScope and the Australian Government via the National Collaborative
606 Research Infrastructure Strategy. We thank O. Tschauner for editorial handling, and F. Yin, C.
607 Ma, and I. Baziotis for constructive comments.

608 **REFERENCES CITED**

609 Abate, B., Koeberl, C., Kruger, F.J., and Underwood, J.R. Jr. (1999) BP and Oasis impact
610 structures, Libya, and their relation to Libyan Desert Glass, in Dressler, B.O and Sharpoton, V.L.
611 (eds.) Large Meteorite Impacts and Planetary Evolution II, Boulder, Colorado, Geological
612 Society of America Special Paper, 339, 177-192.

613

614 Ainslie, N.G., Mackenzie, J.D., and Turnbull, D. (1961) Melting kinetics of quartz and
615 cristobalite. Journal of Physical Chemistry, 65, 1718-1724.
616
617 Aramendia, J., Gomez-Nubla, L., Fdez-Ortiz de Vallejuelo, S., Castro, K., Murelaga, X., and
618 Madariaga, J.M. (2011) New findings by Raman microspectroscopy in the bulk and inclusions
619 trapped in Libyan Desert Glass. Spectroscopy Letters, 44, 521-525.
620
621 Barnes, V.E., and Underwood, J.R. Jr. (1976) New investigations of the strew field of Libyan
622 desert glass and its petrography. Earth and Planetary Science Letters, 30, 117-122.
623
624 Barrat, J.A., Jahn, B.M., Amosse, J., Rocchia, R., Keller, F., Poupea, G.R., and Diemer, E.
625 (1997) Geochemistry and origin of Libyan Desert glasses. Geochimica et Cosmochimica Acta,
626 61, 1953-1959.
627
628 Benzerara, K., Guyot, F., Barrat, J.A., Gillet, P., and Lesourd, M. (2002) Cristobalite inclusions
629 in the Tatahouine achondrite: Implications for shock conditions. American Mineralogist, 87,
630 250–1256.
631
632 Beran, A., and Koeberl, C. (1997) Water in tektites and impact glasses by fourier-transformed
633 infrared spectrometry. Meteoritics and Planetary Science, 32, 211-216.
634
635 Breneman, R.C. and Halloran, J.W. (2014) Kinetics of cristobalite formation in sintered silica.
636 Journal of the American Ceramic Society, 97, 2272-2278.

637

638 Brückner, R. (1970) Properties and structure of vitreous silica. I. Journal of Non-Crystalline
639 Solids, 5, 123-175.

640

641 Cavosie, A.J., Koeberl, C. (2019) Overestimation of threat from 100 Mt-class airbursts? High-
642 pressure evidence from zircon in Libyan Desert Glass. Geology, 47, 609-612.

643

644 Cavosie, A.J., Timms, N.E., Erickson, T.M., Hagerty, J.J., and Hörz, F. (2016) Transformations
645 to granular zircon revealed: Twinning, reidite, and ZrO_2 in shocked zircon from Meteor Crater
646 (Arizona, USA). Geology, 44, 703-706.

647

648 Cavosie, A.J., Timms, N.E., Ferrière, L., and Rochette, P. (2018a) FRIGN zircon- The only
649 terrestrial mineral diagnostic of high-pressure and high-temperature shock deformation.
650 Geology, 46, 891-894.

651

652 Cavosie, A.J., Timms, N.E., Erickson, T.M., and Koeberl, C. (2018b) New clues from Earth's
653 most elusive impact crater: Evidence of reidite in Australasian tektites from Thailand. Geology,
654 46, 203-206.

655

656 Cayron, C., Artaud, B., and Briottet, L. (2006) Reconstruction of parent grains from EBSD data.
657 Materials Characterization, 57, 386-401.

658

659 Christensen, N.H., Cooper, A.R., and Rawal, B.S. (1973) Kinetics of dendritic precipitation of
660 cristobalite from a potassium silicate melt. Journal of the American Ceramic Society, 56, 557-
661 561.
662
663 Christie, J.M., Lally, J.S., Heuer, A.H., Fisher, R.M., Griggs, D.T., and Radcliffe, S.V. (1971)
664 Comparative electron petrography of Apollo 11, Apollo 12, and terrestrial rocks. Proceedings of
665 the Second Lunar Science Conference, 1, 69-89, New York, Pergamon.
666
667 Crespo, T.M., Lozano Fernandez, R.P., and Gonzalez Laguna, R. (2009) The fulgurite of Torre
668 de Moncorvo (Portugal): description and analysis of the glass. European Journal of Mineralogy,
669 21, 783-794.
670
671 Damby, D.E., Llewellin, E.W., Horwell, C.J., Williamson, B.J., Najorka, J., Cressey, G., and
672 Carpenter, M. (2014) The α-β phase transition in volcanic cristobalite. Journal of Applied
673 Crystallography, 47, 1205-1215.
674
675 Darling, R.S., Chou, I.-M., and Bodnar, R.J. (1997) An occurrence of metastable cristobalite in
676 high-pressure garnet granulite. Science, 276, 91-93.
677
678 Dollase, W.A. (1965) Reinvestigation of the structure of low cristobalite. Zeitschrift für
679 Kristallographie, 121, 369-377.
680
681 Erickson, T.M., Pearce, M.A., Reddy, S.M., Timms, N.E., Cavosie, A.J., Bourdet, J., Rickard,

W.D.A., and Nemchin, A.A. (2017) Microstructural constraints on the mechanisms of the transformation to reidite in naturally shocked zircon. Contributions to Mineralogy and Petrology, 172(6), doi:10.1007/s00410-016-1322-0.

Erickson, T.M., Timms, N.E., Pearce, M.A., Cayron, C., Deutsch, A., Keller, L.P., and Kring, D.A. (2019) Shock-produced high-pressure (La,Ce,Th)PO_4 polymorph revealed by microstructural phase heritage of monazite. Geology, 47, 505-508. https://doi/org/10.1130.G46008.1.

Ferrière, L., Koeberl, C., and Reimold, W.U. (2009) Characterisation of ballen quartz and cristobalite in impact breccias: new observations and constraints on ballen formation. European Journal of Mineralogy, 21, 203–217.

Francois-Saint-Cyr, H.G., Stevie, F.A., McKinley, J.M., Elshot, K. Chow, L., and Richardson, K.A. (2003) Diffusion of 18 elements implanted into thermally grown SiO_2. Journal of Applied Physics, 94, 7433-7439.

Frischat, G.H., Klopfer, C., Beier, W., and Weeks, R.A. (1984) Some properties of Libyan Desert Glasses. Journal of Non-Crystalline Solids, 67, 621-628.

Frischat, G.H., Schwander, R., Beier, W., and Weeks, R.A. (1989) High-temperature thermal expansion of Libyan Desert Glass as compared to that of silica glasses and natural silicates. Geochimica et Cosmochimica Acta, 53, 2731-2733.

Fröhlich, F., Poupeau, G., Badou, A., Le Bourdonnec, F.X., Sacquin, Y., Dubernet, S., Bardintzeff, J.M., Véran, M., Smith, D.C., and Diemer, E. (2013) Libyan Desert Glass: New field and Fourier transform infrared data. Meteoritics and Planetary Science, 48, 2517-2530.

Greshake, A., Koeberl, C., Fritz, J., and Reimold, W.U. (2010) Brownish inclusion and dark streaks in Libyan Desert Glass: Evidence for high-temperature melting of the target rock. Meteoritics and Planetary Science, 45, 973-989.

Greshake, A., Wirth, R., Fritz, J., Jakubowski, T., and Bottger, U. (2018) Mullite in Libyan Desert Glass: Evidence for high-temperature/low-pressure formation. Meteoritics and Planetary Science, 53, 467-481.

Grieg, J.W., Merwin, H.E., and Shepherd, E.S. (1936) Notes on the volatile transport of silica. American Journal of Science, 25, 61-73.

Gucsik, A., Koeberl, C., Brandstätter, F., Libowitzky, E., and Zhang, M. (2004) Infrared, Raman, and cathodoluminescence studies of impact glasses. Meteoritics and Planetary Science, 39, 1273-1285.

Hammer, J.E. (2008) Experimental studies of the kinetics and energetics of magma crystallization. Reviews in Mineralogy and Geochemistry, 69, 9-59.

728 Hatch, D.M., and Ghose, S. (1991) The α-ß phase transition in cristobalite, SiO_2. Physics and
729 Chemistry of Minerals, 17, 554-562.
730
731 Heaney, P.J. (1994) Structure and chemistry of the low-pressure silica polymorphs. Reviews in
732 Mineralogy, 29, 1-40.
733
734 Horwell, C.J., Williamson, B.J., Llewellin, E.W., Damby, D.E., and Le Blond, J.S. (2013) The
735 nature and formation of cristobalite at the Soufriere Hills volcano, Montserrat: implications for
736 the petrology and stability of silicic lava domes. Bulletin of Volcanology, 75, 696,
737 doi.org/10.1007/s00445-013-0696-3.
738
739 Humbert, M., Gey, N., Patapy, C., Joussein, E., Huger, M., Guinebretiere, R., Chotard, T., and
740 Hazotte, A. (2010) Identification and orientation determination of parent cubic domains from
741 electron backscatter diffraction maps of monoclinic pure zirconia. Scripta Materialia, 63, 411-
742 414.
743
744 Jackson, K.A. (1967) Current concepts in crystal growth from the melt. Progress in Solid State
745 Chemistry, 4, 53-56.
746
747 Jambon, A., Lussiez, P., Clocchiatti, R., Weisz, J., and Hernandez, J. (1992) Olivine growth rates
748 in a tholeiitic basalt: An experimental study of melt inclusions in plagioclase. Chemical Geology,
749 96, 277-287.
750

751 Kayama, M., Nishido, H., and Ninagawa, K. (2009) Effect of impurities on cathodoluminescence
752 of tridymite and cristobalite. Journal of Mineralogical and Petrological Sciences, 104, 401-406.
753
754 Keith, T.E.C., and Muffler, L.J.P. (1978) Minerals produced during cooling and hydrothermal
755 alteration of ash flow tuff from Yellowstone drill hole Y-5. Journal of Volcanology and
756 Geothermal Research, 3, 373-402.
757
758 Kerschhofer, L., Schärer, U., and Deutsch, A. (2000) Evidence for crystals from the lower
759 mantle: baddeleyite megacrysts of the Mbuji Mayi kimberlite. Earth and Planetary Science
760 Letters, 179, 219–225.
761
762 Kirkpatrick, R.J. (1975) Crystal growth from the melt: A review. American Mineralogist, 60,
763 798-814.
764
765 Kirkpatrick, R.J. (1981) Kinetics of crystallization of igneous rocks. Reviews in Mineralogy, 8,
766 321-398.
767
768 Kleinmann, B. (1969) The breakdown of zircon observed in the Libyan desert glass as evidence
769 of its impact origin. Earth and Planetary Science Letters, 5, 497-501.
770
771 Koeberl, C. (1997) Libyan Desert Glass: Geochemical composition and origin. In V. De
772 Michele, Ed., Proceedings of the Silica ’96 Meeting on Libyan Desert Glass and related desert
773 events, p. 121–131. Segrate (Milan), Pyramids.

774

775 Koeberl, C. (2000) Confirmation of a meteoritic component in Libyan Desert Glass from
776 osmium-isotopic data. Meteoritics and Planetary Science, 35, A89–A90.

777

778 Koeberl, C. and Ferrière, L. (2019) Libyan Desert Glass area in western Egypt: Shocked quartz
779 in bedrock points to possible presence of a deeply eroded impact structure in the region.
780 Meteoritics and Planetary Science, 54, 2398-2408.

781

782 Kuebler, K.E. (2013) A combined electron microprobe (EMP) and Raman spectroscopic study of
783 the alteration products in Martian meteorite MIL 03346. Journal of Geophysical Research, 118,
784 347-368.

785

786 Kuroda, T., Irisawa, T., and Ookawa, A. (1977) Growth of a polyhedral crystal from solution and
787 its morphological stability. Journal of Crystal Growth, 42, 41-46.

788

789 Leroux, H. and Cordier, P. (2006) Magmatic cristobalite and quartz in the NWA 856 Martian
790 meteorite. Meteoritics and Planetary Science, 41, 913-923.

791

792 Lofgren, G. (1971) Experimentally produced devitrification textures in natural rhyolitic glass.
793 Geological Society of America Bulletin, 82, 111-124.

794

795 Lussier, A.J., Rouvimov, S., Burns, P.C., and Simonetti, A. (2017) Nuclear-blast induced
796 nanotextures in quartz and zircon within Trinitite. American Mineralogist, 102, 445-460.

Macris, C.A., Asimow, P.D., Badro, J., Eiler, J.M., Zhang, Y., and Stolper, E.M. (2018) Seconds after impact: Insights into the thermal history of impact ejecta from diffusion between lechatelierite and host glass in tektites and experiments. Geochimica et Cosmochimica Acta, 241, 69-94.

Magna, T., Deutsch, A., Mezger, K., Skála, R., Seitz, H.-M., Mizera, J., Řanda, Z. and Adolph, L. (2011) Lithium in tektites and impact glasses: Implications for sources, histories and large impacts. Geochimica et Cosmochimica Acta, 75, 2137-2158.

McArthur, A.N., Cas, R.A.F., and Orton, G.J. (1998) Distribution and significance of crystalline, perlitic and vesicular textures in the Ordovician Garth Tuff (Wales). Bulletin of Volcanology, 60, 260-285.

Milman-Barris, M.S., Beckett, J.R., Baker, M.B., Hofmann, A.E., Morgan, Z., Crowley, M.R., Vielzeuf, D., and Stolper, E. (2008) Zoning of phosphorus in igneous olivine. Contributions to Mineralogy and Petrology, 155, 739-765.

Moynihan, C.T., Easleal, A.J., Wilder, J., and Tucker, J. (1974) Dependence of the glass transition temperature on heating and cooling rate. Journal of Physical Chemistry, 78, 2673-2677.

819 Nord, G.L. Jr. (1992) Imaging transformation-induced microstructures. Reviews in Mineralogy,
820 27, 455-508.
821
822 Nord, G.L. Jr. (1994) Transformation-induced twin boundaries in minerals. Phase Transitions,
823 48, 107-134.
824
825 Pasek, M.A. and Pasek, V.D. (2018) The forensics of fulgurite formation. Mineralogy and
826 Petrology, 112, 185-198.
827
828 Pearce, M. and Escolme, A (2021) Phase heritage during replacement reactions in Ti-bearing
829 minerals. Contributions to Mineralogy and Petrology, 176, 21. https://doi.org/10.1007/s00410-
830 021-01775-8
831
832 Pratesi, G., Viti, C., Cipriani, C., and Mellini, M. (2002) Silicate-silicate liquid immiscibility and
833 graphite ribbons in Libyan desert glass. Geochimica et Cosmochimica Acta, 66, 903-911.
834
835 Richet, P., Bottinga, Y., Denielou, L., Petitet, J.P., and Tequi, C. (1982) Thermodynamic
836 properties of quartz, cristobalite, and amorphous SiO_2: drop calorimetry measurements between
837 1000 and 1800 K and a review from 0 to 2000 K. Geochimica et Cosmochimica Acta, 46, 2639-
838 2658.
839
840 Rogers, A.F. (1922) A new occurrence of cristobalite in California. American Mineralogist, 30,
841 211-216.

842

843 Schipper, C.I., Rickard, W.D.A., Reddy, S.M., Saxey, D.W., Castro, J.M., Fougerouse, D.,
844 Quadir, Z., Conway, C., Prior, D.J., and Lilly, K. (2020) Volcanic SiO_2-cristobalite: A natural
845 product of chemical vapor deposition. American Mineralogist, 105, 510-524.

846

847 Seebaugh, W.R., Kinser, D.L., Hoff, R., and Weeks, R.A. (1985) Cooling and crystallization
848 rates of Libyan desert glass. Journal of Non-Crystalline Solids, 71, 387-395.

849

850 Shoval, S., Champagnon, B., and Panczer, G. (1997) The quartz-cristobalite transformation in
851 heated chert rock composed of micro and crypto-quartz by micro-Raman and FT-IR
852 spectroscopic methods. Journal of Thermal Analysis, 50, 203-213.

853

854 Sighinolfi, G.P., Lugli, F., Piccione, F., Michele, V.D., and Cipriani, A. (2020) Terrestrial target
855 and melting site of Libyan Desert Glass: New evidence from trace elements and Sr isotopes.
856 Meteoritics and Planetary Science, 55, 1865-1883.

857

858 Spencer, L.J. (1939) Tektites and silica-glass. Mineralogical Magazine, 167, 425-442.

859

860 Svetsov, V., Shuvalov, V. and Kosarev, I. (2020) Formation of Libyan desert glass: Numerical
861 simulations of melting of silica due to radiation from near-surface airbursts. Meteoritics and
862 Planetary Science, 55, 895-910.

863

Swaenen, M., Stefaniak, E.A., Frost, R., Worobiec, A., and Van Grieken, R. (2010) Investigation of inclusions trapped inside Libyan desert glass by Raman microscopy. Analytical and Bioanalytical Chemistry, 397, 2659-2665.

Swamy, V., Saxena, S.K., Sundman, B., and Zhang, J. (1994) A thermodynamic assessment of silica phase diagram. Journal of Geophysical Research, Solid Earth, 99 (B6), 11787–11794.

Swanson, S.E., and Fenn, P.M. (1986) Quartz crystallization in igneous rocks. American Mineralogist, 71, 331-342.

Swanson, S.E., Naney, M.T., Westrich, H.R., and Eichelberger, J.C. (1989) Crystallization history of Obsidian Dome, Inyo Domes, California. Bulletin of Volcanolgy, 5, 161-176.

Taylor, S.R., McLennan, S.M. (1995) The geochemical evolution of the continental crust. Reviews of Geophysics, 33, 241-265.

Timms, N.E., Erickson, T.M., Pearce, M.A., Cavosie, A.J., Schmieder, M., Tohver, E., Reddy, S.M., Zanetti, M.R., and Nemchin, A.A. (2017a) A pressure-temperature phase diagram for zircon at extreme conditions. Earth-Science Reviews, 165, 185-202.

Timms, N.E., Erickson, T.M., Zanetti, M.R., Pearce, M.A., Cayron, C., Cavosie, A.J., Reddy, S.M., Wittmann, A., and Carpenter, P.K. (2017b) Cubic zirconia in >2370 °C impact melt records Earth's hottest crust. Earth and Planetary Science Letters, 477, 52-58.

Trepmann, C.A., Dellefant, F., Kaliwoda, M., Hess, K.-U., Schmahl, W.W., and Hölzl, S. (2020) Quartz and cristobalite ballen in impact melt rocks from the Ries impact structure, Germany, formed by dehydration of shock-generated amorphous phases. Meteoritics and Planetary Science 55, 2360-2374, doi:10.1111/maps.13590.

Wagstaff, F.E. (1968) Crystallization kinetics of internally nucleated vitreous silica. Journal of the American Ceramic Society, 51, 449-452.

Wagstaff, F.E. (1969) Crystallization and melting kinetics of cristobalite. Journal of the American Ceramic Society, 52, 650-654.

Watkins, J., Manga, M., Huber, C., and Martin, M. (2009) Diffusion-controlled spherulite growth in obsidian inferred from H_2O concentration profiles. Contributions to Mineralogy and Petrology, 157, 163–172. DOI 10.1007/s00410-008-0327-8.

Watson, E.B. and Muller, T. (2009) Non-equilibrium isotopic and elemental fractionation during diffusion-controlled crystal growth under static and dynamic conditions. Chemical Geology, 267, 111-124.

Watson, E.B., Cherniak, D.J., and Holycross, M.E. (2015) Diffusion of phosphorus in olivine and molten basalt. American Mineralogist, 100, 2053-2065.

Welsch, B., Hammer, J., and Hellebrand, E. (2014) Phosphorus zoning reveals dendritic architecture of olivine. Geology, 42, 867-870.

White, L.F., Darling, J.R., Moser, D.E., Cayron, C., Barker, I., Dunlop, J., and Tait, K.T. (2018) Baddeleyite as a widespread and sensitive indicator of meteorite bombardment in planetary crusts. Geology, 46, 719-722.

Whittington, A.G., Sehlke, A., and Speck, A.K. (2021) Recalescence in silicate melts: Applications to circumstellar dust grains, lava fountains, and lava flows. Lunar and Planetary Science Conference, abstract 1776, LPI Contribution no. 2548.

Withers, R.L., Thompson, J.G., and Welberry, T.R. (1989) The structure and microstructure of α-cristobalite and its relationship to ß-cristobalite. Physics and Chemistry of Minerals, 16, 517-523.

Zhao, S., Yang, M., Xu, H., and Zhang, S. (2008) Branching and twinning in α-cristobalite dendrites: an electron backscatter diffraction study. Journal of Applied Crystallography, 41, 800-802.

Figure captions

Figure 1. Cathodoluminescence images of Libyan Desert Glass. A. Sample LDG-2018-2a, showing layering. B. Sample LDG-2018-2b; inset shows the cristobalite grain in Figure 2A.

Figure 2. Cristobalite grains. A. Cathodoluminescence (CL) image showing a zoned LDG cristobalite grain with a rim and radial features extending from the core, sample LDG-2018-02b. B & C. CL images of LDG cristobalite grains described in the text. White arrows indicate the glass-rim and core-rim boundary. D. Optical image of β-cristobalite grain experimentally nucleated in vitreous silica from 1350-1620 °C (no scale bar available) [Used by permission of Wiley, from Wagstaff (1968), Journal of the America Chemical Society, vol. 51, No. 8, Fig. 6, p. 452].

Figure 3. Cristobalite grain L4, sample LDG-2018-4. A. Secondary electron image (bright spots are charging artifacts). B. Backscattered electron image. C. Cathodoluminescence (CL) image. Long-dash line indicates the boundary between CL light layer (above) and CL dark layer (below). D. EDS-Al distribution map. In B, C, and D the short-dash outline is the grain boundary.

Figure 4. Orientation maps of cristobalite grain L4. A. Pattern quality (Band contrast, BC) map. B. Orientation data shown with an inverse pole figure (IPFz) color scheme. C. Pole figures of twin domains 1-3. D. Pole figures of twin domains 4-6. Stereonets are equal area, lower hemisphere projections in the sample reference frame. Circled data on stereonets indicate shared orientations.

Figure 5. Twin systematics in grain L4. A. Orientation data in an inverse pole figure (IPFz) color scheme. B. Stereonet showing six {112} planes in domain 1-3 (labelled a-f). C. Images from A showing orientation of the intersection of six twin planes from domain 1-3

(labelled a-f). D. Image from A showing orientation of twin plane (labelled g) forming the boundary between domains 1-3 and 4-6. E. Stereonet showing crystallographic relations of the twin plane (g), and graphical representation of the disorientation relationship of 70°/<100> measured by EBSD (dashed arrows indicate direction). F. Image from A showing dendritic twin domains in rim. Arrows indicate elongation direction.

Figure 6. Time-of-flight secondary ion mass spectrometry (ToF-SIMS) maps of Al distribution in grain L4 with a "heat map" color scale, where red represents a higher signal intensity than yellow. A. Images in CL, Al (EDS), and orientation (IPFz) of areas analyzed by ToF-SIMS. B. ToF-SIMS map of Al distribution in the rim. C, D. ToF-SIMS map of Al distribution in the core. E. Images in CL, Al (EDS), and orientation (IPFz) of additional areas analyzed by ToF-SIMS. F-H. ToF-SIMS maps of Al distribution across the core-rim boundary.

Figure 7. Elemental abundances along a linear transect orthogonal to layering in LDG. A: Silica variation across dark and light cathodoluminescence (CL) domains. B: CL image of LDG showing location of EMPA (10 μm) and LAICPMS analysis spots (50 μm). Analyses shown include LAICPMS spots 1-10 (Table 3) and EMPA spots 1-21 (Table 1). Dashed lines indicate layer boundaries. C: Variation in element abundances across dark and light CL domains.

Figure 8. Analysis of cristobalite grain L4 by EMPA and LAICPMS. A: Location of analysis sites on CL (above) and Al-EDS (below) maps. B: Covariation of SiO_2 and Al_2O_3 for grain L4 (EMPA, Table 2) grouped by core-rim (top) and CL domain (bottom). The lower panel includes EMPA data from Greshake et al. (2010, 2018). C: Covariation of Fe and Al in

978 cristobalite grain L4 (LAICPMS, Table 4), showing a correlation between dark and light CL
979 layers.
980
981 Figure 9. Element abundances for LDG and cristobalite grain L4. A. LAICPMS data
982 from this study (Tables 3 and 4). Data indicated 'CL dark' are from the CL dark layer in LDG
983 (n=6) that contains grain L4 (n=6), and data indicated 'CL light' are from the CL light layer in
984 LDG (n=4) that contains grain L4 (n=14). B. Composition of LDG from this study compared to
985 other samples. Upper continental crust (UCC) values from Taylor and MacLennan (1995).
986
987 Figure 10. Inclusions in the core of grain L4. A. Al abundance map (from Figure 3D)
988 showing oscillatory zoning defined by Al. B. Backscattered electron (BSE) image of sub-vertical
989 inclusion arrays from an Al-rich layer in the core (see location in A). Dashed lines indicate twin
990 boundaries. C. Area from B, showing polyphase sub-micrometer inclusions. D. Al abundance
991 map (EDS) showing inclusions are Al-rich.
992
993 Figure 11. Stability fields of silica polymorphs and melt at low pressure (after Swamy et
994 al., 1994). Vertical arrows indicate heating and cooling paths for LDG; numbers are temperature
995 estimates (references in text). For brevity, only the thermal history of LDG (heating and cooling)
996 is considered; high-pressure conditions (e.g., Cavosie and Koeberl, 2019) were not present
997 during cristobalite crystallization.
998
999 Figure 12. Crystallographic relations of the ß- to α-cristobalite transformation. A parent
1000 cubic crystal (left) gives rise to three tetragonal orientation variants (right). Stereonets are equal

area, lower hemisphere projects, and show orientations of models in reference frames where either (001) or {110} is vertical. Cubic crystal morphology after Wagstaff (1968). Tetragonal crystal forms are from Mindat.org.

Figure 13. Model of ß-cristobalite origin in Libyan Desert Glass (LDG). A. Silica-rich precursor material (quartz arenite?), pre-impact. Grey and black grains represent Al-bearing phases. B. Rapid superheating of the precursor formed layered silica melt. C. Crystallization of magmatic ß-cristobalite octahedra with various growth zoning features defined by Al zonation in supercooled silica melt. D. Dendritic growth of ß-cristobalite rims by devitrification in the solid-state. E. Fracturing due to volume change (ΔV) from the ß-α transformation. F. Formation of α-cristobalite twins; twins in the rim extend across and pre-date fractures; twins in the core are pinned, forming after fractures.

This is the peer-reviewed, final accepted version for American Mineralogist, published by the Mineralogical Society of America.
The published version is subject to change. Cite as Authors (Year) Title. American Mineralogist, in press.
DOI: https://doi.org/10.2138/am-2021-7922. http://www.minsocam.org/

Table 1. Electron microprobe analysis of Libyan Desert Glass sample LDG-2018-4 (in wt%).

	Oxide	SiO_2	Al_2O_3	FeO	TiO_2	K_2O	Na_2O	CaO	MgO	MnO	Cr_2O_3	P_2O_5	SO_3	Total
	dl[a]	0.02	0.02	0.05	0.02	0.01	0.02	0.02	0.01	0.05	0.02	0.05	0.03	-
#	CL[b]													
1	dark	97.5	1.30	0.23	0.16	0.03	bdl[c]	bdl	bdl	bdl	bdl	bdl	bdl	99.3
2	dark	97.5	1.18	0.25	0.10	0.02	bdl	bdl	bdl	bdl	bdl	bdl	bdl	99.1
3	mixed	97.3	1.24	0.12	0.16	0.02	bdl	0.02	bdl	bdl	bdl	bdl	bdl	98.9
4	dark	97.3	1.17	0.21	0.14	0.02	bdl	bdl	0.01	bdl	bdl	bdl	bdl	98.9
5	dark	96.9	1.31	0.23	0.14	0.03	bdl	bdl	0.01	bdl	bdl	bdl	0.03	98.6
6	dark	96.6	1.57	0.27	0.17	0.02	bdl	bdl	0.01	bdl	bdl	bdl	bdl	98.7
7	dark	99.3	1.18	0.21	0.08	0.02	bdl	bdl	bdl	bdl	bdl	bdl	bdl	100.8
8	mixed	100.8	0.31	0.08	0.05	bdl	bdl	bdl	0.01	bdl	bdl	bdl	0.03	101.2
9	light	99.0	1.59	0.13	0.20	0.01	bdl	0.03	0.01	bdl	bdl	bdl	0.03	101.1
10	light	99.9	0.69	0.10	0.18	0.03	bdl	0.03	bdl	bdl	bdl	0.05	bdl	101.0
11	light	99.2	1.37	0.22	0.23	0.02	0.02	bdl	0.01	bdl	bdl	bdl	bdl	101.1
12	light	99.8	0.52	0.07	0.13	bdl	bdl	bdl	0.02	bdl	bdl	bdl	bdl	100.5
13	dark	98.9	1.24	0.18	0.11	0.01	bdl	bdl	0.01	bdl	0.02	bdl	bdl	100.4
14	dark	98.4	1.52	0.24	0.16	0.02	bdl	bdl	bdl	bdl	bdl	bdl	0.03	100.4
15	mixed	98.3	1.43	0.13	0.19	bdl	bdl	bdl	bdl	bdl	bdl	bdl	bdl	100.1
16	light	99.3	0.65	0.08	0.11	0.01	bdl	bdl	0.01	bdl	bdl	bdl	bdl	100.2
17	light	98.1	1.19	0.12	0.14	0.06	0.02	bdl	0.01	bdl	bdl	bdl	bdl	99.6
18	light	98.8	0.69	0.08	0.11	0.01	bdl	bdl	0.01	bdl	bdl	bdl	bdl	99.7
19	light	98.8	0.64	0.11	0.11	bdl	bdl	0.02	0.01	bdl	bdl	bdl	bdl	99.7
20	light	98.7	0.60	0.06	0.16	bdl	0.02	bdl	0.01	0.08	bdl	bdl	bdl	99.7
21	dark	97.3	1.48	0.15	0.17	0.02	0.03	bdl	bdl	bdl	bdl	bdl	bdl	99.1
Average, all		98.5	1.09	0.16	0.14	0.02	bdl	bdl	0.01	bdl	bdl	bdl	bdl	99.9
	2SD[d]	2.18	0.78	0.14	0.08	0.03	-	-	0.01	-	-	-	-	1.71
Avgerage, CL light (n=9)														
		99.1	0.88	0.11	0.15	0.02	bdl	bdl	0.01	bdl	bdl	bdl	bdl	100.3
	2SD	1.15	0.78	0.10	0.08	0.04	-	-	0.01	-	-	-	-	1.30
Average, CL dark (n=9)														
		97.8	1.33	0.22	0.14	0.02	bdl	bdl	0.01	bdl	bdl	bdl	bdl	99.5
	2SD	1.84	0.32	0.08	0.06	0.01	-	-	0.00	-	-	-	-	1.66

Note(s): The CL light and dark layers were not correlated with optically visible layering.

Data in this table are shown in Figure 7A. The EMPA spot size used is 10 µm across.

[a]dl = detection limit.

[b]CL = cathodoluminescence response (intensity) of area analyzed.

[c]bdl = below dl; [d]SD = standard deviation.

This is the peer-reviewed, final accepted version for American Mineralogist, published by the Mineralogical Society of America.
The published version is subject to change. Cite as Authors (Year) Title. American Mineralogist, in press.
DOI: https://doi.org/10.2138/am-2021-7922. http://www.minsocam.org/

Table 2. Electron microprobe analysis of cristobalite grain L4 in sample LDG-2018-4 (in wt%).

	Oxide	SiO_2	Al_2O_3	FeO	TiO_2	K_2O	Na_2O	CaO	MgO	MnO	Cr_2O_3	P_2O_5	SO_3	Total
	dl[a]	0.02	0.02	0.05	0.02	0.01	0.02	0.02	0.01	0.05	0.02	0.05	0.03	-
Core spot	CL[b]													
3	light	100.5	0.34	0.10	0.15	bdl[c]	bdl	bdl	bdl	bdl	bdl	bdl	bdl	101.1
4	dark	99.0	1.49	0.12	0.14	bdl	bdl	0.04	bdl	bdl	bdl	bdl	bdl	100.8
5	light	100.0	0.57	0.10	0.15	0.01	bdl	bdl	0.02	bdl	bdl	bdl	0.03	101.0
9	light	99.4	0.52	0.10	0.08	bdl	bdl	bdl	bdl	bdl	bdl	0.05	bdl	100.2
Average, core		99.7	0.73	0.11	0.13	bdl	bdl	bdl	bdl	bdl	bdl	bdl	bdl	100.8
Rim spot	CL													
1	dark	98.1	1.94	0.29	0.22	bdl	bdl	0.03	0.01	0.06	bdl	bdl	0.03	100.7
2	dark	98.6	1.69	0.25	0.17	bdl	0.02	0.05	0.02	bdl	bdl	bdl	bdl	100.9
6	light	100.1	0.58	0.08	0.12	bdl	bdl	bdl	bdl	bdl	bdl	bdl	bdl	101.0
7	light	98.9	0.49	0.10	0.13	0.02	bdl	bdl	bdl	bdl	bdl	bdl	bdl	99.7
8	light	100.1	0.52	0.06	0.10	bdl	bdl	bdl	bdl	bdl	bdl	0.05	0.03	100.9
Average, rim		99.2	1.04	0.15	0.15	bdl	bdl	bdl	bdl	bdl	bdl	bdl	bdl	100.6
Average, all		99.4	0.91	0.13	0.14	bdl	bdl	bdl	bdl	bdl	bdl	bdl	bdl	100.7
	2SD[d]	1.62	1.23	0.16	0.08	-	-	-	-	-	-	-	-	0.92
Avgerage, CL light (n=6)														
		99.9	0.50	0.09	0.12	0.02	bdl	bdl	bdl	bdl	bdl	bdl	bdl	100.6
	2SD	1.16	0.17	0.03	0.05	0.02	-	-	-	-	-	-	-	1.15
Average, CL dark (n=3)														
		98.6	1.71	0.22	0.18	bdl	bdl	0.04	0.02	bdl	bdl	bdl	bdl	100.8
	2SD	0.83	0.45	0.17	0.08	-	-	0.02	0.02	-	-	-	-	0.16

Note(s): The CL light and dark layers were not correlated with optically visible layering.
Data in this table are shown in Figure 8B. The EMPA spot size used is 10 µm across.

[a]dl = detection limit.

[b]CL = cathodoluminescence response (intensity) of area analyzed.

[c]bdl = below dl; [d]SD = standard deviation.

This is the peer-reviewed, final accepted version for American Mineralogist, published by the Mineralogical Society of America.
The published version is subject to change. Cite as Authors (Year) Title. American Mineralogist, in press.
DOI: https://doi.org/10.2138/am-2021-7922. http://www.minsocam.org/

Table 3. Trace element abundances in Libyan Desert Glass sample LDG-2018-4 by LAICPMS (in ppm).

	dl[a]	1	2	3	4	5	6	7	8	9	10	11	12	13	14	15	16	17	18	19	20	21	22	23	24	25	Avg	2SD[b]	Avg	Avg
CL[c]		dark	dark	dark	dark	light	light	dark	light	light	light	dark	light	dark	dark	dark	light	dark	dark	dark	dark	mixed	dark	dark	dark	light	all		CL light	CL dark
Li	0.05	2.92	3.20	3.20	3.65	2.09	1.69	3.22	1.98	1.77	2.95	5.03	1.92	3.40	3.09	3.38	2.05	4.55	5.09	4.98	1.59	3.25	4.15	4.20	4.28	2.70	3.21	2.13	2.14	3.75
B	0.4	7.41	7.87	8.02	8.82	9.64	11.0	7.78	8.46	7.45	8.75	7.83	5.83	7.19	8.13	7.82	10.0	7.84	7.71	7.54	7.00	9.73	9.70	7.65	8.92	9.88	8.32	2.27	8.87	7.95
Na	0.8	19.0	20.6	20.8	24.3	12.4	10.6	20.7	12.3	11.0	20.5	32.9	12.1	21.3	21.0	22.3	11.6	29.7	33.7	31.2	8.7	19.4	26.0	26.7	26.8	16.3	20.5	14.3	13.3	24.1
Mg	0.2	30.6	31.9	35.8	30.9	21.9	21.4	32.5	19.8	16.2	33.8	23.6	13.9	30.8	34.0	40.8	20.6	43.5	34.9	26.7	12.4	26.9	29.7	37.5	34.4	24.7	28.4	15.9	21.6	31.9
Al	0.2	7440	8280	8250	9200	4030	2860	8300	4550	3410	7180	8490	2830	7240	8760	10000	3320	10600	10200	8340	1700	5630	8380	9650	9300	5080	6920	5260	4160	8380
K	1	118	130	130	153	80.4	62.6	126	73.3	66.6	127	184	64.7	128	128	145	70.7	173	188	178	44.8	112	156	156	163	101	122	82.8	80.8	144
Ca	40	51.0	76.0	68.0	87.0	55.0	bdl[d]	bdl	82.0	47.0	110	83.0	65.0	101	65.0	54.0	45.0	82.0	104	84.0	bdl	85.0	95.0	76.0	78.0	102	77.0	37.2	72.3	78.9
Sc	0.04	2.08	2.05	2.11	2.13	1.54	1.31	2.12	1.47	1.40	1.91	1.88	1.24	1.93	2.05	2.30	1.44	2.43	2.23	1.87	1.05	1.63	1.99	2.22	2.11	1.52	1.84	0.73	1.48	2.04
Ti	0.1	995	1070	1070	1420	1130	745	1020	860	642	1050	1150	508	924	1050	1040	964	1180	1150	1150	262	1020	1680	1130	1310	1250	1030	556	894	1100
V	0.02	6.77	7.48	7.91	7.21	3.89	3.14	7.61	3.93	2.93	5.45	5.66	2.11	6.33	7.68	8.99	3.53	9.73	8.75	5.18	1.72	5.47	5.96	8.86	7.26	4.62	5.93	4.43	3.70	7.07
Cr	0.2	6.33	5.96	7.11	6.69	3.18	3.22	6.00	3.43	3.14	6.16	5.40	3.62	6.86	6.70	7.59	3.41	8.66	6.87	5.57	3.05	5.10	5.57	7.49	6.86	4.28	5.53	3.27	3.81	6.42
Mn	0.3	7.17	7.15	6.96	9.75	8.27	6.06	6.55	7.21	4.94	9.30	6.62	4.37	6.81	6.61	8.48	8.25	8.13	7.37	7.81	2.69	7.61	12.4	7.75	10.6	10.6	7.58	3.98	7.38	7.67
Fe	2	1620	1680	1810	1600	876	747	1550	688	520	1010	1190	453	1490	1730	2100	809	2270	1830	1130	463	1250	1400	1920	1790	1020	1320	1040	765	1600
Co	0.01	0.157	0.177	0.176	0.232	0.130	0.107	0.192	0.115	0.105	0.173	0.150	0.103	0.171	0.156	0.218	0.121	0.257	0.222	0.211	0.038	0.181	0.268	0.186	0.233	0.132	0.168	0.107	0.123	0.190
Ni	0.06	0.685	0.700	0.737	1.03	0.430	0.339	0.710	0.445	0.383	0.784	0.679	0.560	0.810	0.601	0.749	0.268	0.705	0.917	0.758	0.238	0.570	0.726	0.706	0.760	0.365	0.626	0.396	0.447	0.719
Cu	0.02	1.48	1.74	1.84	2.12	1.00	0.933	1.76	1.02	0.890	1.58	2.68	0.992	1.72	1.80	1.85	1.04	2.60	2.79	2.49	0.76	1.63	2.17	2.22	2.24	1.31	1.71	1.19	1.10	2.02
Zn	0.08	2.26	2.45	2.84	2.54	1.49	1.24	2.46	1.24	1.01	2.08	1.95	1.24	2.59	2.49	2.96	1.55	3.24	2.74	1.85	0.96	1.91	2.34	2.96	2.70	1.55	2.11	1.32	1.43	2.46
Rb	0.02	0.528	0.576	0.577	0.548	0.263	0.252	0.496	0.230	0.205	0.384	0.374	0.230	0.524	0.657	0.675	0.252	0.627	0.538	0.425	0.149	0.331	0.418	0.582	0.571	0.270	0.427	0.317	0.261	0.517
Sr	0.01	23.0	23.4	24.1	26.6	21.6	21.5	22.6	22.2	15.1	31.3	23.0	14.9	21.7	22.6	28.8	22.0	28.9	25.2	26.3	6.24	22.8	29.5	25.5	28.0	26.6	23.3	10.3	21.9	24.1
Y	0.001	5.70	5.93	5.92	6.43	4.99	4.40	5.72	5.10	3.67	5.70	6.08	2.91	5.08	6.11	6.69	5.58	6.72	6.52	6.00	2.25	5.47	6.93	6.50	6.48	5.22	5.52	2.29	4.70	5.94
Zr	0.01	163	171	167	238	208	153	171	183	134	200	210	112	162	173	153	193	174	178	227	54.8	189	319	176	231	233	183	95.7	177	185
Nb	0.001	2.63	2.89	2.88	3.56	2.71	1.94	2.73	2.43	1.76	2.91	3.11	1.44	2.48	3.01	2.97	2.37	3.28	3.25	3.17	0.814	2.73	4.12	3.15	3.57	3.13	2.76	1.38	2.34	2.97
Ba	0.01	20.7	22.2	22.4	22.7	19.2	19.2	23.1	18.2	13.8	22.8	20.5	11.8	20.6	21.7	25.4	20.0	25.6	24.1	21.4	10.9	20.6	23.5	24.4	23.7	20.3	20.7	7.40	18.2	22.0
La	0.001	9.90	10.4	10.3	11.2	8.94	9.09	10.4	9.74	6.48	10.4	10.73	5.36	9.37	10.7	11.3	14.1	11.6	11.4	10.7	4.85	9.54	11.8	11.1	11.6	9.43	10.0	3.94	9.20	10.5
Ce	0.001	21.7	22.6	22.5	24.6	20.2	20.5	22.5	21.8	15.4	23.3	24.1	12.6	20.6	23.5	25.0	33.1	25.6	25.4	24.1	11.4	21.8	26.1	24.5	25.6	21.3	22.4	8.61	21.0	23.1
Pr	0.001	2.22	2.31	2.31	2.46	1.97	1.94	2.32	2.09	1.45	2.26	2.42	1.18	2.10	2.41	2.54	3.33	2.58	2.60	2.40	1.09	2.05	2.63	2.46	2.56	2.08	2.23	0.921	2.04	2.34
Nd	0.005	8.34	8.36	8.29	9.03	6.87	6.94	8.44	7.70	5.31	8.23	8.70	4.39	7.44	8.64	9.58	11.4	9.73	9.49	8.83	3.68	7.62	9.59	9.23	9.37	7.34	8.10	3.36	7.28	8.55
Sm	0.01	1.51	1.48	1.46	1.72	1.30	1.24	1.55	1.38	1.01	1.53	1.59	0.856	1.41	1.73	1.72	2.03	1.79	1.71	1.61	0.644	1.45	1.79	1.66	1.73	1.39	1.49	0.604	1.34	1.57
Eu	0.002	0.254	0.270	0.299	0.307	0.230	0.233	0.270	0.254	0.193	0.334	0.275	0.166	0.249	0.302	0.324	0.242	0.324	0.301	0.321	0.091	0.251	0.361	0.328	0.342	0.247	0.271	0.119	0.237	0.289
Gd	0.01	1.16	1.32	1.30	1.34	1.12	1.09	1.23	1.33	0.85	1.21	1.27	0.687	1.02	1.41	1.41	1.33	1.40	1.44	1.29	0.600	1.18	1.40	1.42	1.30	1.12	1.21	0.434	1.09	1.27
Dy	0.003	0.983	1.09	1.14	1.12	0.92	0.87	1.00	0.97	0.69	1.01	1.01	0.502	0.95	1.13	1.18	1.04	1.27	1.15	1.03	0.438	1.06	1.21	1.15	1.12	0.916	1.00	0.393	0.865	1.06
Er	0.002	0.561	0.587	0.613	0.697	0.484	0.406	0.586	0.518	0.367	0.606	0.603	0.303	0.531	0.654	0.708	0.552	0.731	0.691	0.605	0.207	0.556	0.737	0.703	0.718	0.549	0.571	0.265	0.473	0.621
Yb	0.01	0.562	0.604	0.569	0.723	0.491	0.427	0.590	0.487	0.382	0.539	0.671	0.298	0.560	0.650	0.718	0.455	0.655	0.709	0.596	0.189	0.514	0.769	0.574	0.633	0.605	0.559	0.265	0.461	0.611
Hf	0.003	4.10	4.33	4.45	5.98	5.31	3.94	4.33	4.70	3.42	4.94	5.30	2.78	4.10	4.59	3.99	4.84	4.57	4.46	5.95	1.38	4.74	8.19	4.73	6.02	5.97	4.68	2.47	4.49	4.78
Pb	0.01	5.08	5.51	5.59	6.60	4.58	4.09	5.14	4.91	3.59	6.36	6.37	3.75	5.37	5.21	5.86	4.48	6.93	6.28	6.44	2.47	5.14	6.94	5.65	6.54	4.71	5.34	2.20	4.56	5.75
Th	0.001	3.45	3.73	3.65	4.58	3.40	2.87	3.53	2.96	2.23	3.80	4.02	1.69	3.12	3.83	3.83	3.63	4.02	4.00	4.04	1.26	3.69	5.60	4.02	4.63	3.73	3.57	1.76	3.04	3.83
U	0.001	1.04	1.12	1.14	1.30	1.00	0.866	1.09	0.945	0.77	1.17	1.17	0.584	1.02	1.13	1.17	1.08	1.25	1.27	1.21	0.430	1.12	1.40	1.22	1.28	1.08	1.07	0.432	0.938	1.14
Sum		10587	11617	11712	12929	6551	4730	11376	6605	4948	9899	11523	4147	10243	12120	13733	5597	14738	13893	11331	2614	8482	12274	13345	13115	7980				

Average of sum, analyses in CL light areas (n=8): 6300 ppm

Average of sum, analyses in CL dark areas (n=16): 11,700 ppm

Note(s): The CL light and dark layers were not correlated with optically visible layering. Data in this table are shown in Figures 7B,C and 9A,B. The LAICPMS spot size used is 50 µm.

[a]dl = detection limit; [b]SD = standard deviation; [c]CL = cathodoluminescence response (intensity) of area analyzed; [d]bdl = below dl.

This is the peer-reviewed, final accepted version for American Mineralogist, published by the Mineralogical Society of America.
The published version is subject to change. Cite as Authors (Year) Title. American Mineralogist, in press.
DOI: https://doi.org/10.2138/am-2021-7922. http://www.minsocam.org/

Table 4. Trace element abundances of cristobalite grain L4 in sample LDG-2018-4 by LAICPMS (in ppm)

	dl[a]	C6[b]	C6r	C7	C7r	C8	C8r	C9	C9r	R10	R10r	R11	R11r	R12	R12r	R13	R13r	Rn1	Rn2	Rn3	Rn4	Avg	Avg	Avg	2SD[c]
CL[d]		light	light	light	light	light	light	light	light	dark	dark	mixed	mixed	dark	dark	light	light	mixed	light	light	light	CL light	CL dark	all	all
Li	0.05	5.81	6.23	8.71	6.51	8.40	7.15	8.40	6.41	4.10	6.31	6.45	5.02	4.49	3.96	10.0	7.47	4.82	5.37	4.00	4.45	6.84	4.72	6.20	3.48
B	0.4	10.2	11.1	10.4	11.5	9.20	9.63	8.40	8.17	8.57	8.18	12.8	10.9	8.05	8.10	10.2	9.27	11.0	10.2	9.68	9.63	9.81	8.23	9.76	2.61
Na	0.8	33.3	27.9	49.0	28.7	46.8	34.5	39.0	29.3	20.6	39.9	34.9	26.0	20.9	18.3	44.4	34.1	23.6	30.0	24.9	25.9	34.4	24.9	31.6	17.6
Mg	0.2	28.5	29.2	20.2	27.1	18.4	20.4	14.5	19.9	41.9	43.0	21.9	24.6	35.3	39.2	21.4	19.2	35.6	25.1	21.7	24.4	22.3	39.9	26.6	16.6
Al	0.2	5520	5600	3260	5130	3190	3220	2380	4130	11400	10600	5000	4320	8770	9510	3780	3080	6840	4120	4560	5130	4080	10100	5480	5230
K	1	9.90	4.14	bdl[e]	5.94	6.00	4.05	bdl	5.06	10.1	213	24.2	62.7	6.40	43.0	9.70	19.3	15.9	59.0	118	87.0	29.9	68.1	39.1	109
Ca	40	179	91.0	125	41.0	bdl	76.0	bdl	67.0	113	78.0	bdl	51.0	bdl	59.0	bdl	76.0	96.0	93.0	65.0	57.0	87.0	83.3	84.5	69.5
Sc	0.04	1.89	2.21	1.63	2.18	1.34	1.81	1.28	1.68	2.46	2.57	1.64	1.84	2.03	2.46	1.55	1.66	2.09	1.69	1.62	1.74	1.71	2.38	1.87	0.73
Ti	0.1	1200	984	1060	1040	961	923	689	789	1260	1140	995	958	1070	1120	747	691	1220	1160	1100	950	946	1150	1000	340
V	0.02	5.60	5.38	4.14	4.92	3.77	3.70	3.23	4.39	10.6	9.51	5.49	4.74	8.60	8.95	4.37	3.31	6.76	4.14	4.24	5.32	4.35	9.41	5.56	4.35
Cr	0.2	4.47	4.61	2.81	4.05	3.31	3.72	2.30	4.25	8.44	7.95	3.97	4.39	8.04	7.42	4.35	3.13	5.38	3.65	3.45	4.47	3.74	7.96	4.71	3.62
Mn	0.3	10.0	8.67	7.90	9.11	7.70	7.59	4.70	6.42	8.39	8.49	6.00	6.98	8.19	7.67	6.81	6.17	11.4	10.1	8.61	6.62	7.72	8.19	7.88	3.17
Fe	2	1210	1090	898	1020	859	816	771	921	2080	2110	1230	1010	1910	1890	1010	749	1450	958	875	1120	946	2000	1200	889
Co	0.01	0.317	0.307	0.319	0.288	0.407	0.340	0.303	0.252	0.312	0.300	0.351	0.367	0.350	0.303	0.271	0.271	0.371	0.446	0.205	0.287	0.309	0.316	0.318	0.109
Ni	0.06	2.32	1.75	3.22	1.75	2.48	1.75	1.97	1.96	0.940	0.846	1.28	1.05	0.850	0.74	3.18	2.45	1.36	1.39	0.630	0.710	1.97	0.844	1.63	1.59
Cu	0.02	7.67	6.52	7.72	6.38	8.09	7.06	8.25	6.31	3.10	4.06	5.83	4.55	3.53	3.02	8.77	7.62	4.78	6.04	3.09	3.33	6.68	3.43	5.79	3.91
Zn	0.08	3.85	2.87	2.63	2.81	3.25	3.02	2.27	2.58	4.00	3.64	3.33	2.85	3.74	3.31	2.95	2.39	3.47	4.60	2.18	2.94	2.95	3.67	3.13	1.24
Rb	0.02	0.083	0.081	0.087	0.109	0.078	0.051	bdl	0.114	0.159	1.06	0.338	0.514	0.102	0.361	0.233	0.264	0.127	0.364	0.490	0.549	0.209	0.421	0.272	0.503
Sr	0.01	24.3	28.9	17.6	28.4	17.9	22.2	13.3	20.9	27.0	28.2	19.5	20.5	22.8	26.4	21.4	18.7	32.7	21.7	22.5	21.3	21.5	26.1	22.8	9.34
Y	0.001	5.09	5.40	4.22	5.53	4.27	4.28	3.35	4.08	6.76	6.76	5.31	5.35	5.60	6.20	4.18	4.43	6.00	4.72	4.80	4.93	4.56	6.33	5.06	1.83
Zr	0.01	185	185	167	204	172	181	135	161	175	172	183	202	164	168	145	142	203	206	204	168	173.0	170	176	42.3
Nb	0.001	3.13	2.76	2.66	2.84	2.82	2.41	1.96	2.16	3.49	3.21	2.63	2.54	3.01	3.01	2.41	1.89	3.20	2.86	2.75	2.61	2.56	3.18	2.72	0.830
Ba	0.01	17.8	18.4	12.5	21.6	14.6	13.9	11.2	16.6	22.4	26.5	24.0	23.9	20.1	26.1	17.5	22.4	23.7	20.1	20.0	20.8	17.5	23.8	19.7	8.75
La	0.001	9.35	9.88	7.88	9.96	8.20	8.01	5.95	7.58	11.6	11.7	9.70	9.97	9.84	10.8	8.41	8.67	10.5	8.48	8.96	9.12	8.50	11.0	9.23	2.81
Ce	0.001	22.2	22.2	20.6	23.2	20.0	18.6	16.2	17.3	27.1	25.8	24.9	22.5	23.7	24.2	22.4	21.3	24.8	20.6	20.7	21.1	20.5	25.2	22.0	5.50
Pr	0.001	2.01	2.12	1.80	2.23	1.82	1.72	1.52	1.66	2.69	2.56	2.19	2.20	2.36	2.40	1.97	1.92	2.37	1.95	1.93	2.03	1.90	2.50	2.07	0.61
Nd	0.005	7.46	7.66	6.36	7.96	6.36	6.22	4.76	5.96	9.61	9.86	8.07	7.88	8.20	9.05	7.46	6.91	8.78	6.31	6.78	7.10	6.72	9.18	7.44	2.59
Sm	0.01	1.32	1.54	1.04	1.48	1.36	1.21	0.780	1.14	1.86	1.77	1.27	1.46	1.44	1.59	1.30	1.28	1.63	1.14	1.26	1.20	1.23	1.67	1.35	0.506
Eu	0.002	0.248	0.289	0.197	0.273	0.192	0.231	0.131	0.193	0.326	0.315	0.242	0.243	0.263	0.303	0.244	0.205	0.298	0.229	0.221	0.242	0.223	0.302	0.244	0.096
Gd	0.01	1.03	1.14	0.770	1.09	0.810	0.937	0.790	0.877	1.45	1.47	0.990	1.23	1.12	1.32	1.04	1.09	1.28	0.917	0.984	1.09	0.966	1.34	1.07	0.403
Dy	0.003	0.790	1.07	0.720	0.986	0.720	0.805	0.620	0.710	1.32	1.24	0.820	0.958	1.01	1.13	0.780	0.819	1.09	0.887	0.882	0.851	0.819	1.17	0.910	0.372
Er	0.002	0.532	0.033	0.474	0.031	0.520	0.036	0.365	0.043	0.713	0.044	0.560	0.049	0.525	0.046	0.491	0.033	0.044	0.035	0.038	0.033	0.205	0.332	0.232	0.500
Yb	0.01	0.430	0.536	0.326	0.516	0.351	0.424	0.381	0.399	0.660	0.598	0.440	0.560	0.510	0.669	0.371	0.458	0.654	0.535	0.478	0.476	0.437	0.609	0.489	0.206
Hf	0.003	4.36	4.81	4.29	4.98	4.25	4.69	3.17	3.92	4.66	4.54	4.70	5.28	4.34	4.18	3.87	3.53	5.10	5.18	5.11	4.32	4.34	4.43	4.46	1.12
Pb	0.01	5.65	5.35	4.56	5.66	5.52	5.08	3.60	4.39	7.14	6.98	5.74	4.96	6.09	6.44	5.13	4.51	6.79	6.19	4.90	4.79	5.03	6.66	5.47	1.87
Th	0.001	3.74	3.63	2.88	4.03	3.05	2.97	2.48	3.08	4.12	4.10	3.64	3.71	3.45	3.90	3.00	2.97	4.10	3.44	3.46	3.32	3.23	3.89	3.45	0.951
U	0.001	1.15	1.05	0.830	1.13	1.03	0.80	0.81	0.919	1.35	1.28	0.96	1.09	1.17	1.19	1.05	1.02	1.26	1.14	1.05	1.02	1.00	1.25	1.06	0.303
Sum		8529	8178	5718	7668	5395	5415	4140	6256	15285	14586	7653	6812	12140	13022	5913	4957	10070	6805	7114	7709	6466	13814	8195	

Average of sum, analyses in CL light areas (n=14): 6705 ppm

Average of sum, analyses in CL dark areas (n=4): 13,758 ppm

Note(s): The CL light and dark layers were not correlated with optically visible layering. Data in this table are shown in Figures 8C and 9A. The LAICPMS spot size used is 50 µm.

Most of the cristobalite grain is in a single, light CL layer (e.g., Figure 3). Only analyses R10 and R12 are in dark CL areas

[a]dl = detection limit; [b]Analysis label convention: C = core; R = rim; r = repeat analysis in same location.

[c]SD = standard deviation; [d]CL = cathodoluminescence response (intensity) of area analyzed; [e]bdl = below dl.

This is the peer-reviewed, final accepted version for American Mineralogist, published by the Mineralogical Society of America.
The published version is subject to change. Cite as Authors (Year) Title. American Mineralogist, in press.
DOI: https://doi.org/10.2138/am-2021-7922. http://www.minsocam.org/

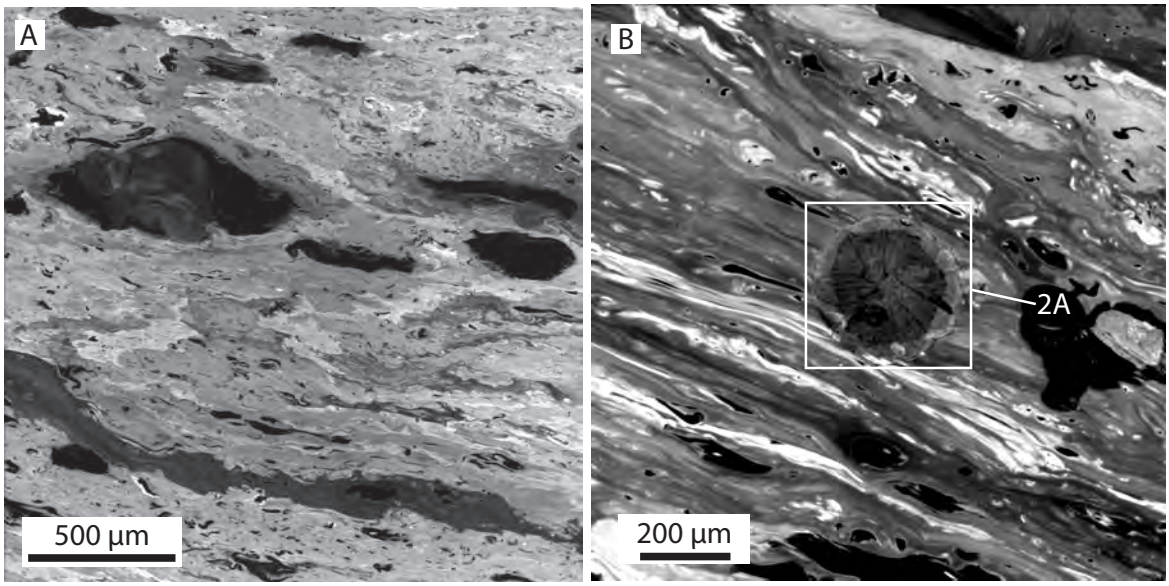

Figure 1

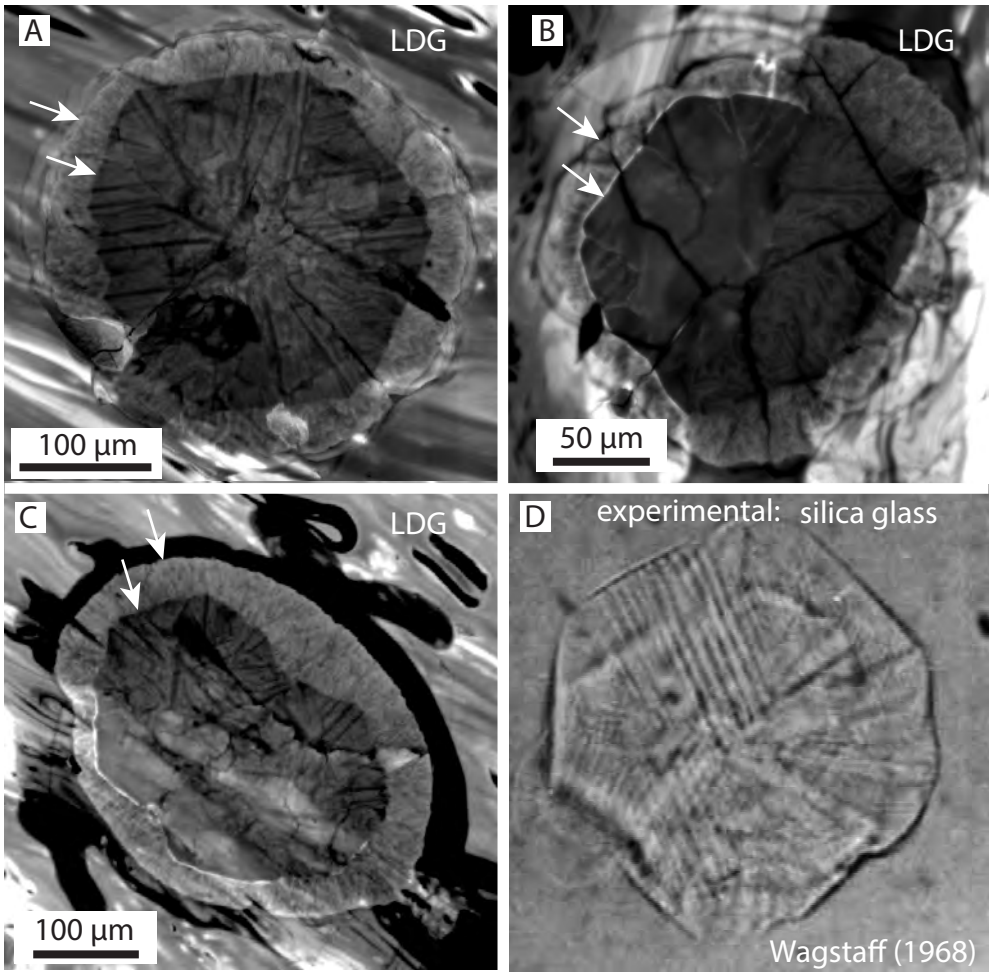

Figure 2

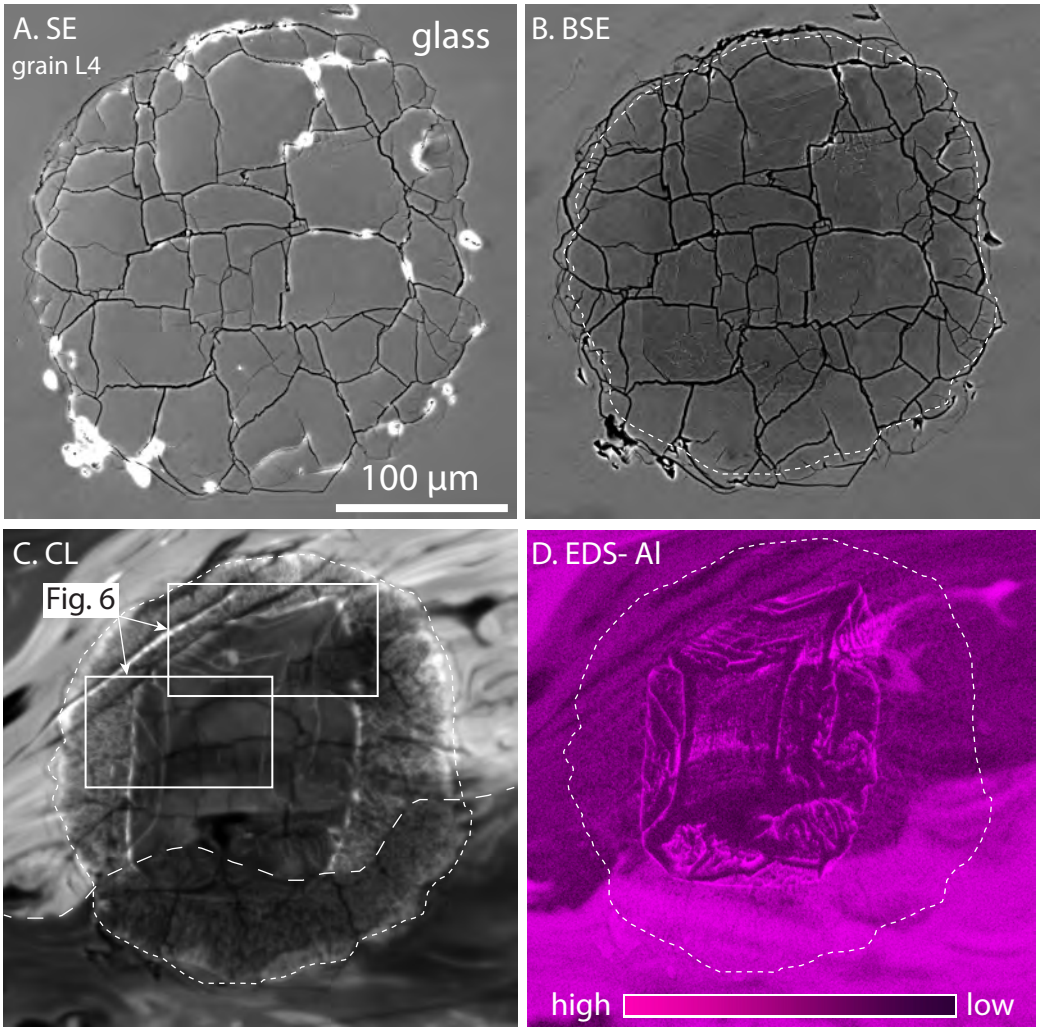

Figure 3

This is the peer-reviewed, final accepted version for American Mineralogist, published by the Mineralogical Society of America.
The published version is subject to change. Cite as Authors (Year) Title. American Mineralogist, in press.
DOI: https://doi.org/10.2138/am-2021-7922. http://www.minsocam.org/

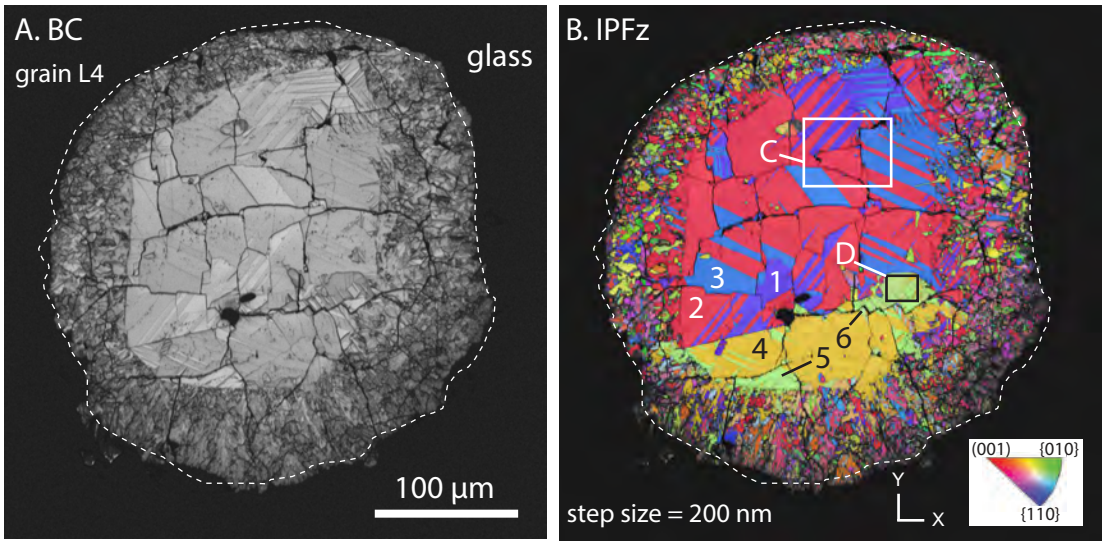

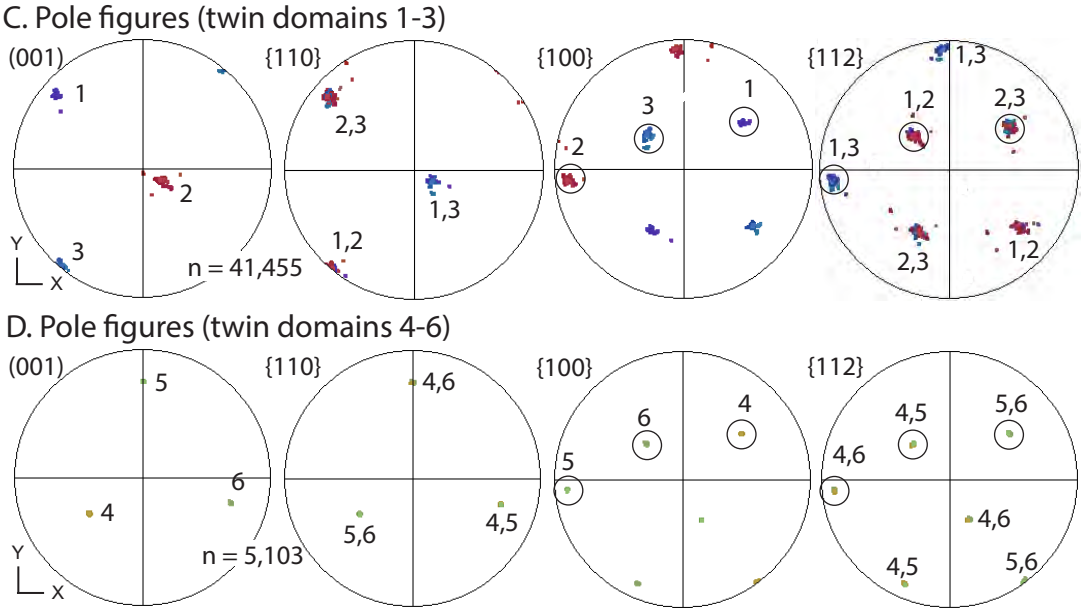

Figure 4

This is the peer-reviewed, final accepted version for American Mineralogist, published by the Mineralogical Society of America.
The published version is subject to change. Cite as Authors (Year) Title. American Mineralogist, in press.
DOI: https://doi.org/10.2138/am-2021-7922. http://www.minsocam.org/

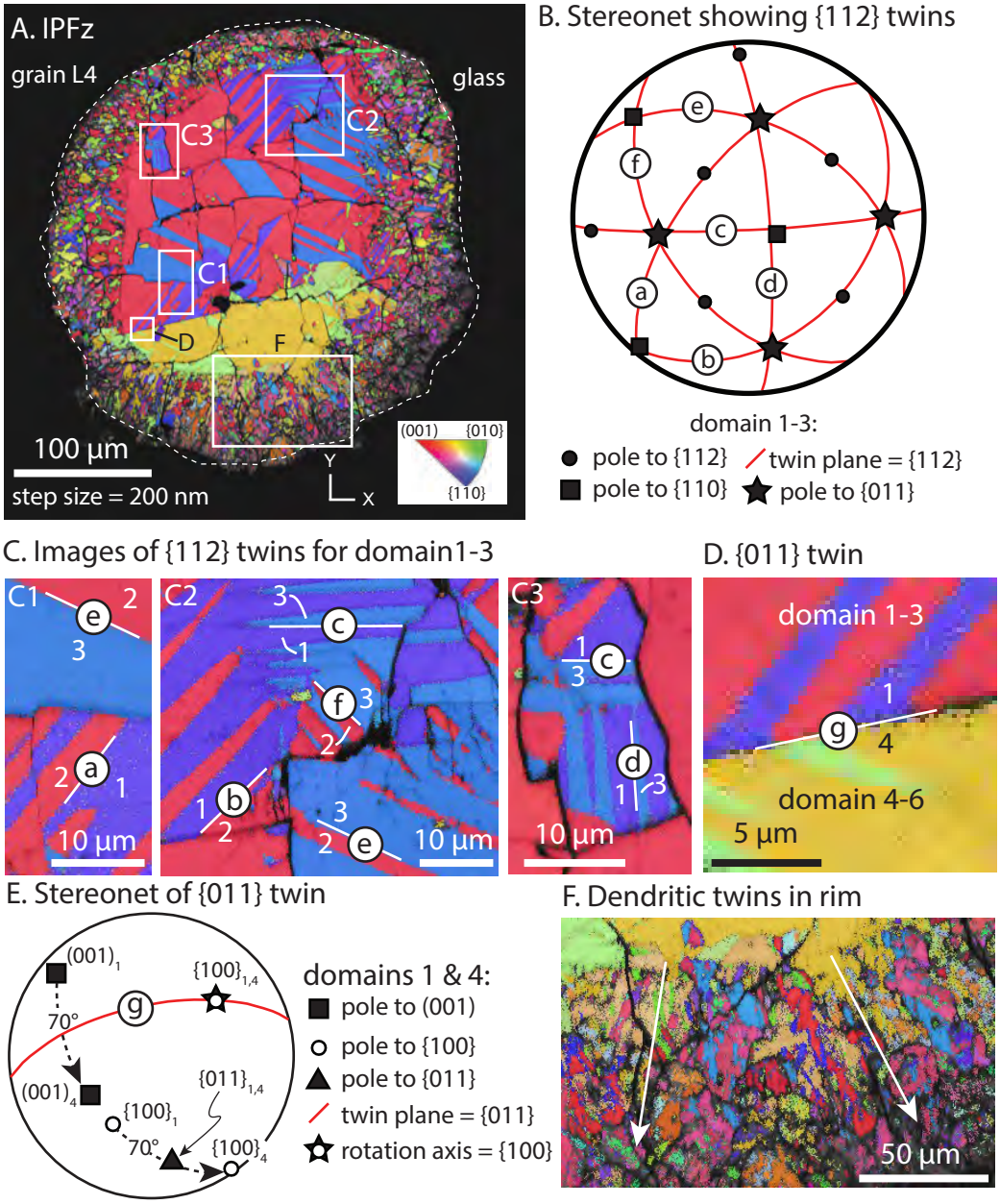

Figure 5

This is the peer-reviewed, final accepted version for American Mineralogist, published by the Mineralogical Society of America.
The published version is subject to change. Cite as Authors (Year) Title. American Mineralogist, in press.
DOI: https://doi.org/10.2138/am-2021-7922. http://www.minsocam.org/

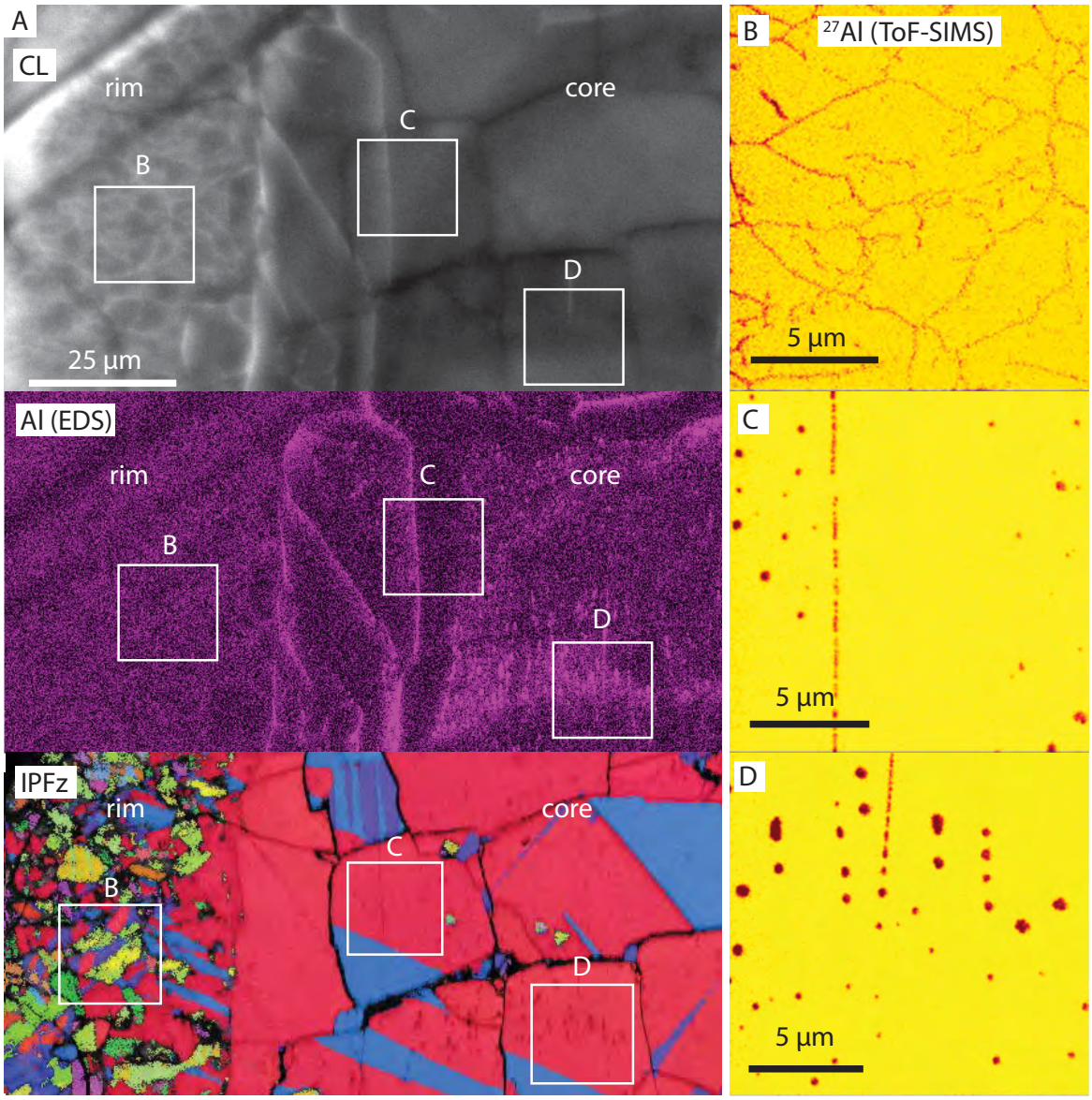

Figure 6

This is the peer-reviewed, final accepted version for American Mineralogist, published by the Mineralogical Society of America.
The published version is subject to change. Cite as Authors (Year) Title. American Mineralogist, in press.
DOI: https://doi.org/10.2138/am-2021-7922. http://www.minsocam.org/

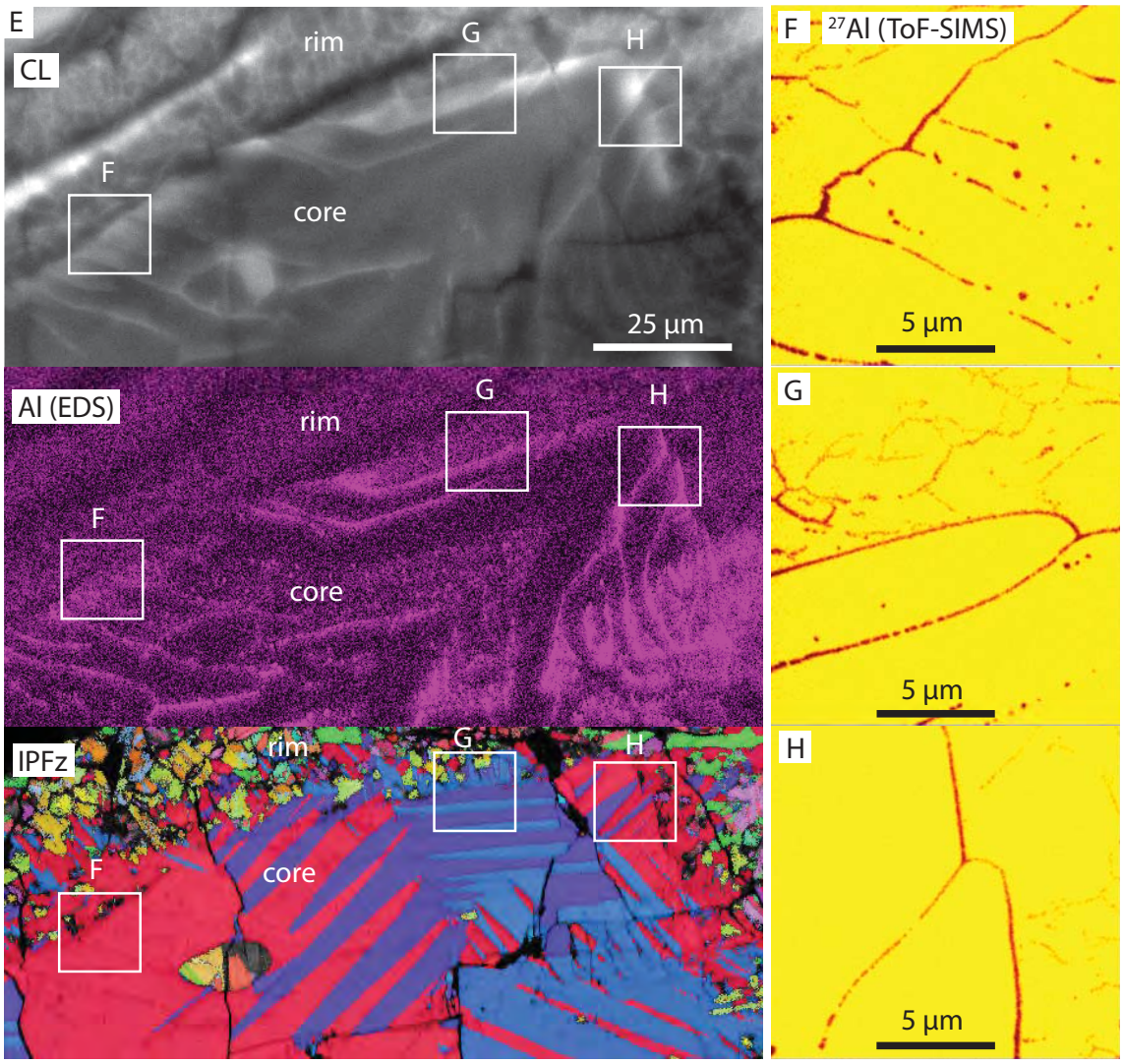

Figure 6 (cont)

This is the peer-reviewed, final accepted version for American Mineralogist, published by the Mineralogical Society of America.
The published version is subject to change. Cite as Authors (Year) Title. American Mineralogist, in press.
DOI: https://doi.org/10.2138/am-2021-7922. http://www.minsocam.org/

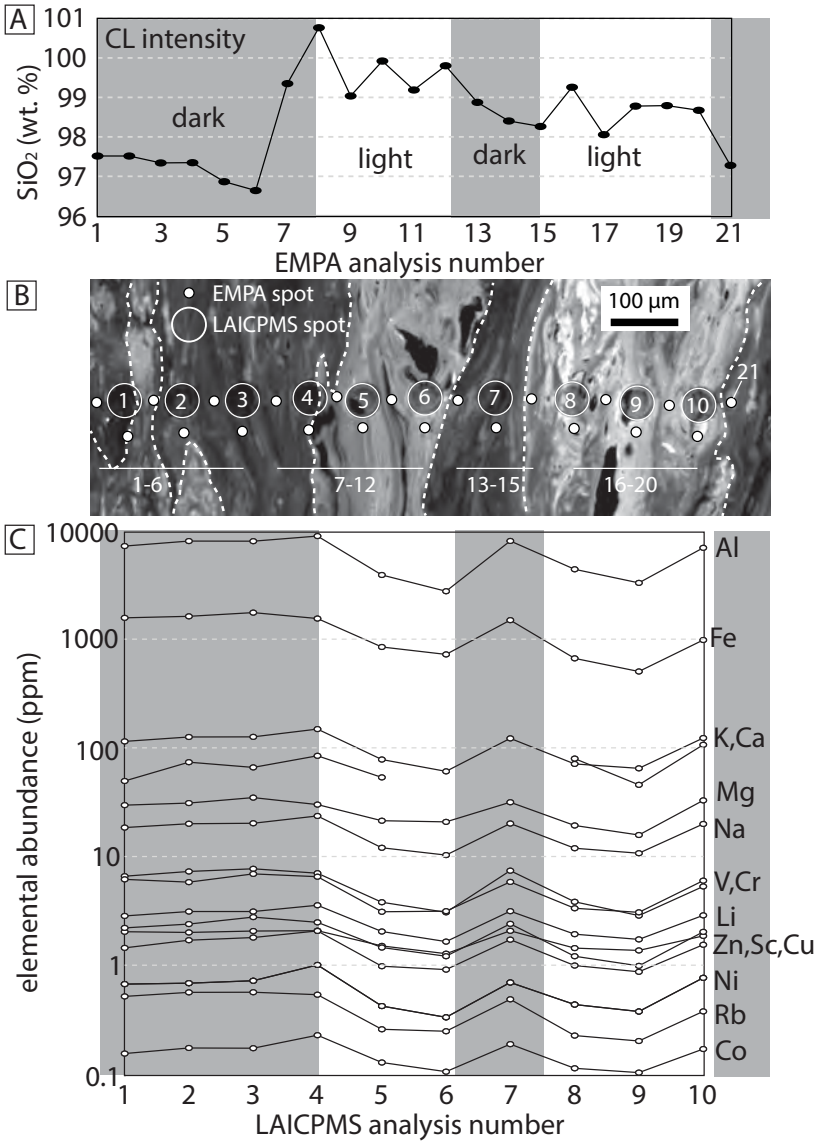

Figure 7

This is the peer-reviewed, final accepted version for American Mineralogist, published by the Mineralogical Society of America.
The published version is subject to change. Cite as Authors (Year) Title. American Mineralogist, in press.
DOI: https://doi.org/10.2138/am-2021-7922. http://www.minsocam.org/

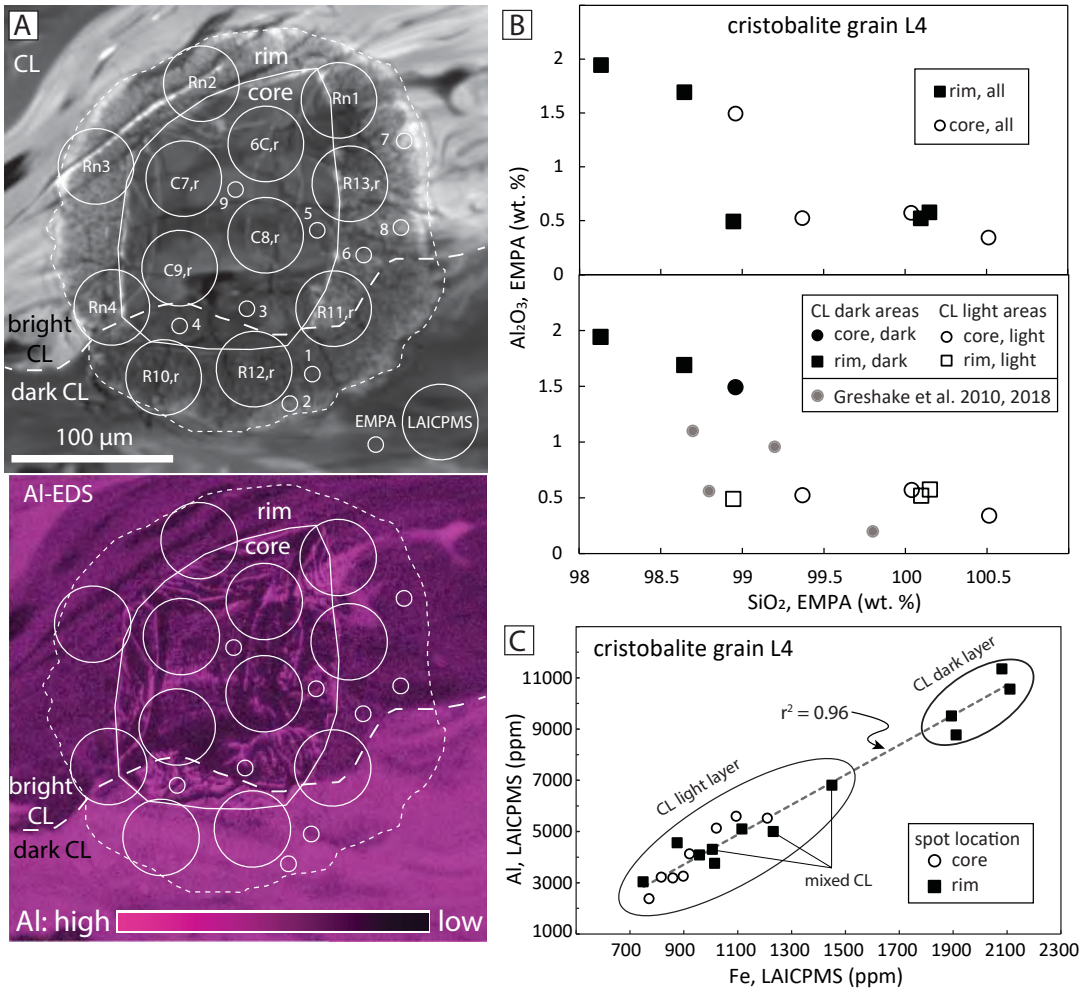

Figure 8

This is the peer-reviewed, final accepted version for American Mineralogist, published by the Mineralogical Society of America.
The published version is subject to change. Cite as Authors (Year) Title. American Mineralogist, in press.
DOI: https://doi.org/10.2138/am-2021-7922. http://www.minsocam.org/

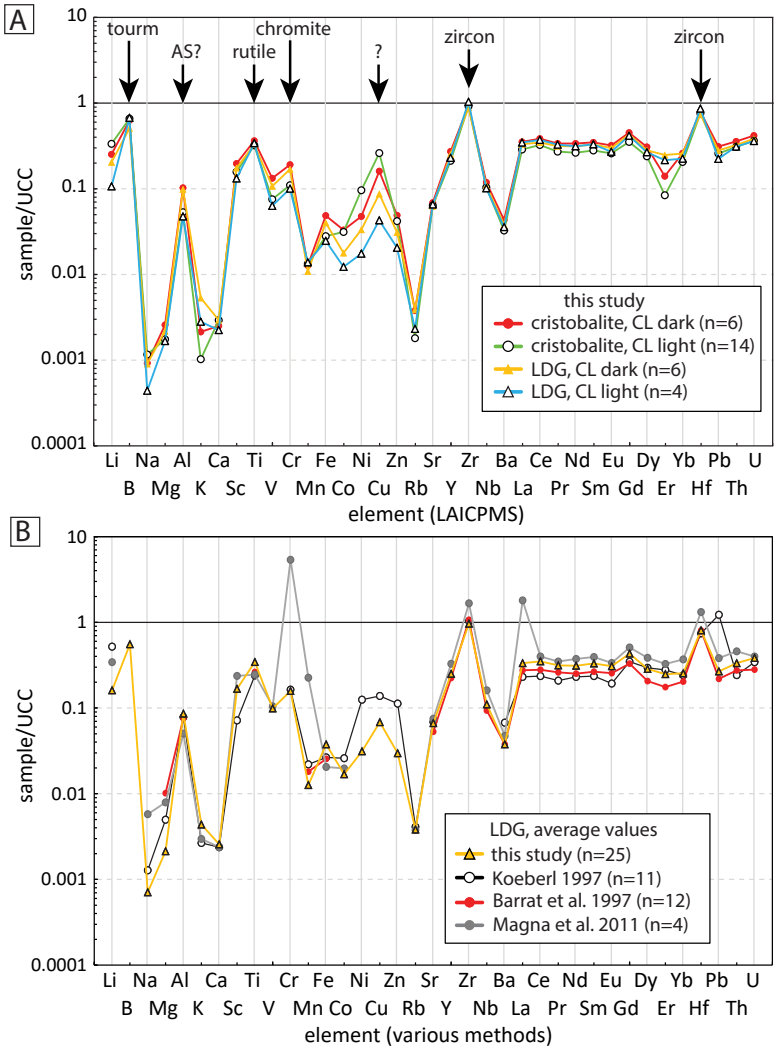

Figure 9

This is the peer-reviewed, final accepted version for American Mineralogist, published by the Mineralogical Society of America.
The published version is subject to change. Cite as Authors (Year) Title. American Mineralogist, in press.
DOI: https://doi.org/10.2138/am-2021-7922. http://www.minsocam.org/

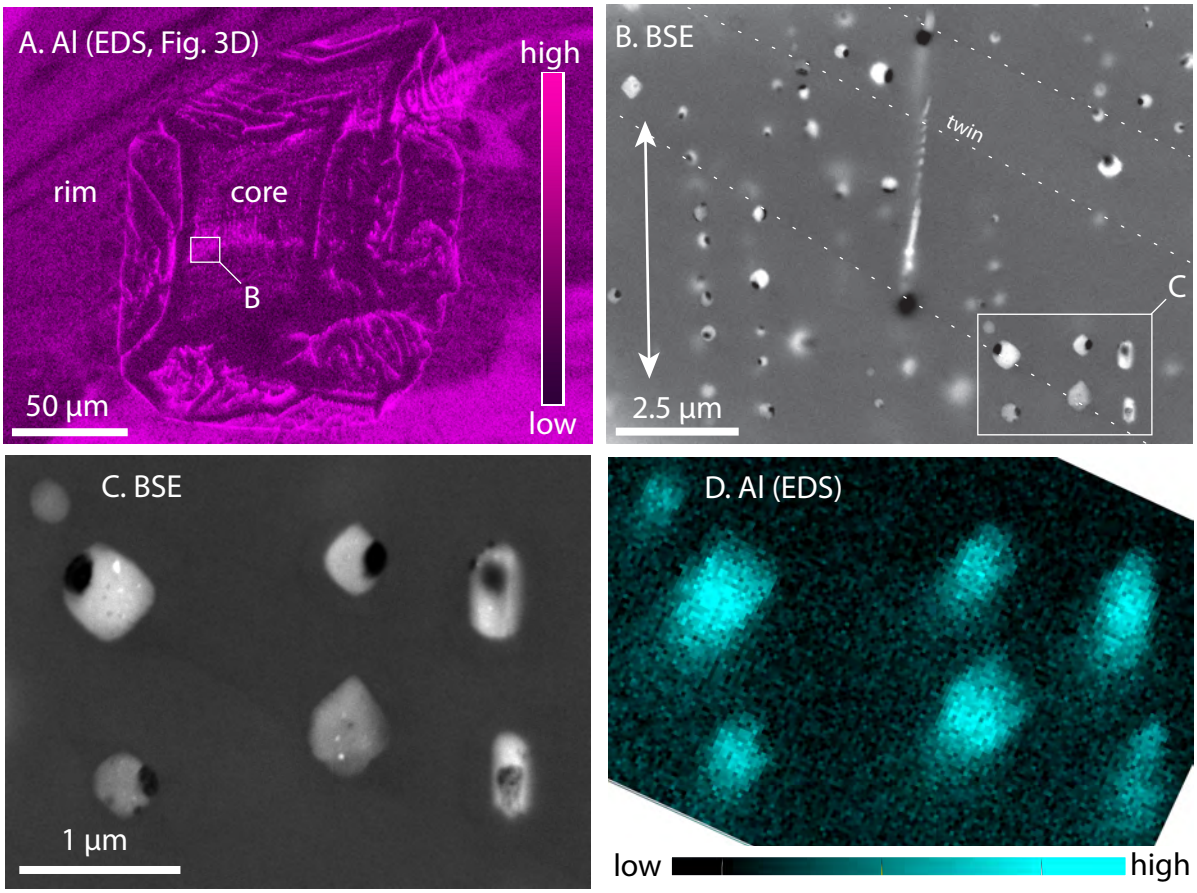

Figure 10

This is the peer-reviewed, final accepted version for American Mineralogist, published by the Mineralogical Society of America.
The published version is subject to change. Cite as Authors (Year) Title. American Mineralogist, in press.
DOI: https://doi.org/10.2138/am-2021-7922. http://www.minsocam.org/

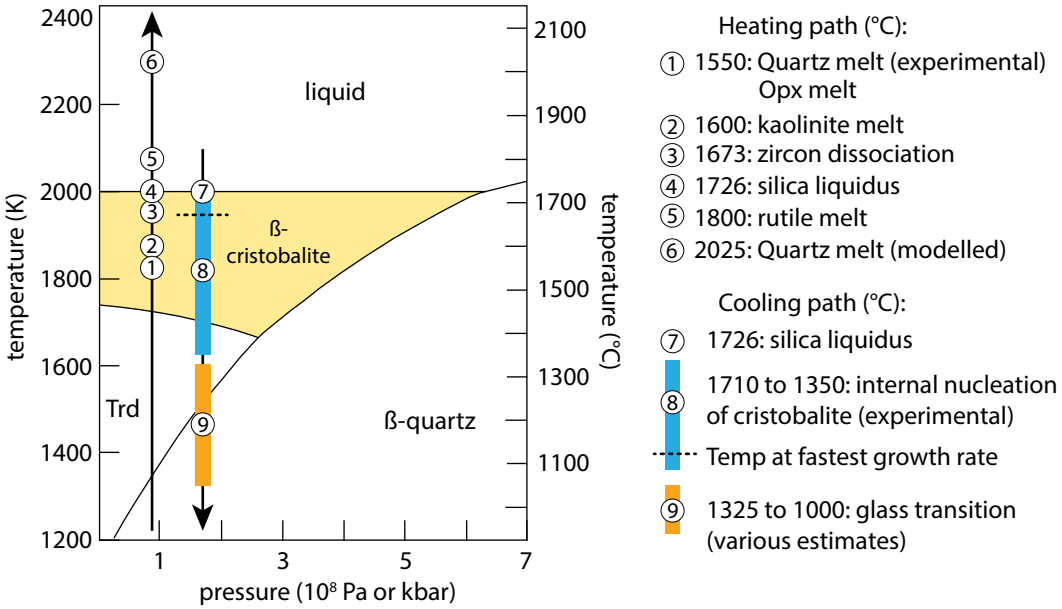

Figure 11

This is the peer-reviewed, final accepted version for American Mineralogist, published by the Mineralogical Society of America.
The published version is subject to change. Cite as Authors (Year) Title. American Mineralogist, in press.
DOI: https://doi.org/10.2138/am-2021-7922. http://www.minsocam.org/

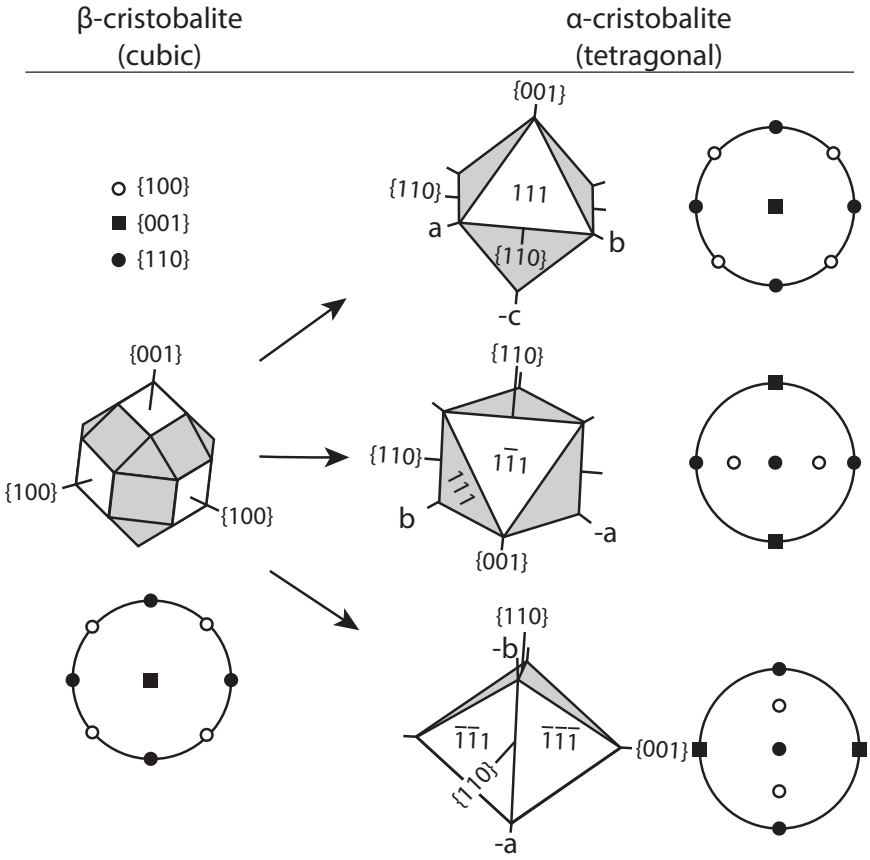

Figure 12

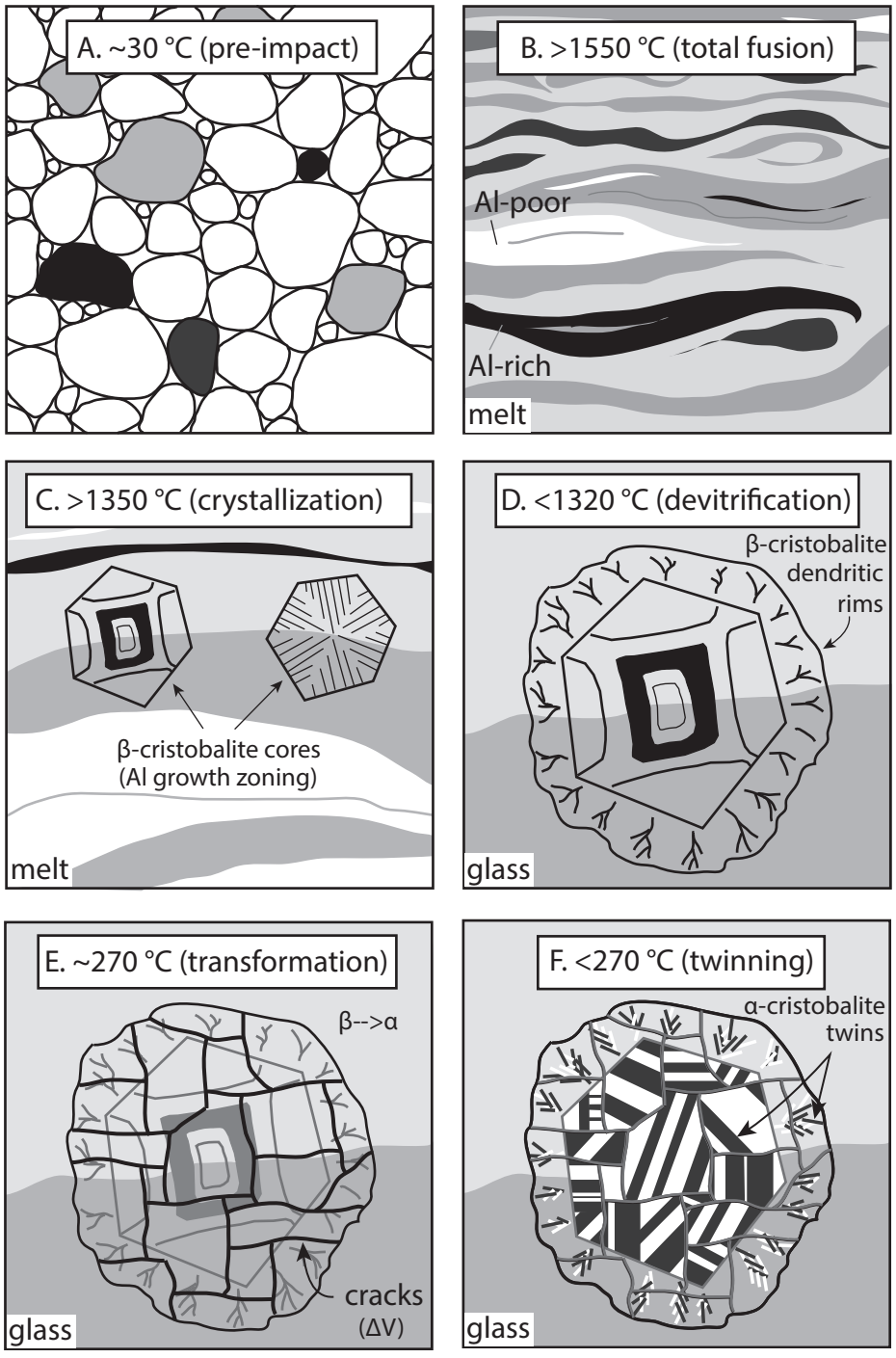

Figure 13